Optical Properties of Nanocomposites

13

Timothy O'Connor and Mikhail Zamkov

Contents

1 Definition of the Topic

Optical characteristics of nanocomposites provide deeper insights into the overall function of these materials. This chapter describes steady-state and time-resolved optical properties of nanocomposites in the UV-Vis range derived through the analysis of a variety of nanoparticle architectures and the extrapolation of general trends from these examples.

2 Overview

Recent progress in controlling the size, morphology, and growth rate of inorganic nanocrystals synthesized via colloidal routes has enabled cost-effective methodologies for the creation of complex nanocomposite systems. These nanostructures are constructed through multistaged syntheses, wherein each step is accompanied by

T. O'Connor (✉) • M. Zamkov
Department of Physics, Bowling Green State University, Bowling Green, USA

Challa S.S.R. Kumar (ed.), *UV-VIS and Photoluminescence Spectroscopy for Nanomaterials Characterization*, DOI 10.1007/978-3-642-27594-4_13,

the addition of a new component, providing a greater degree of control over the optoelectronic properties that govern the overall functionality of the nano-object.

The characteristics of nanocomposites are usually tuned by adjusting the size, shape, and material composition of individual domains as well as the architecture of the overall nanostructure, as electronic interactions across material interfaces strongly contribute into the behavior of the complex nanocrystal.

By analyzing the outcome of steady-state and time-resolved optical measurements, this chapter deciphers the optoelectronic properties of nanocomposites during each stage of the synthesis, providing insights into the mechanism underlying the observed spectral phenomena. Meanwhile, the structural analysis of these nanocomposites using transmission electron microscopy (TEM) adds to procuring a relationship between the observed optical characteristics and the morphology of investigated nanocomposites.

3 Introduction

Inorganic nanocrystals represent one of the most fruitful grounds for the current research in nanoscience and nanotechnology, as they are relevant both to the fundamental understanding of the size- and dimensionality-dependent laws of nanoscale matter and to the bottom-up development of new functional materials, devices, and processes. Unique properties of these nanoparticles arise from the onset of carrier confinement in the two or three dimensions, such that the energy absorbed through optical or electrical excitations can be controllably trapped or channeled within the structure, which gives rise to enormous array of possible applications and new technologies, including lasing [1], photovoltaics, [2, 3] photocatalysis, [4, 5] LEDs, [6–11] bio-labels, [12–14] thermoelectric elements, [15, 16] field-effect transistors, [17–22] magnetic doping, [23, 24] and memory elements. [25–29].

Conjoining two or more materials in a single composite nanocrystal via low-cost colloidal routes further facilitates the design of nanostructures with "adjustable" electronic and optical properties, leading to a new degree of freedom in the development of multifunctional composites. [30–33] Adjacent domains of semiconductors having different band gap values and appropriately chosen band offsets could be used to trap electron–hole pairs in specific regions of the nanocrystal (type I confinement), thus forcing them to recombine therein with high efficiency. Alternatively, composite nanocrystals with a type II alignment of material band gaps, constructed in such a way that band edges of one domain lie lower in energy than the corresponding band edges of the other, facilitate spatial separation of electron–hole pairs (excitons) between different parts of the composite nanostructure, which can be harnessed for the development of photovoltaic and photocatalytic materials [34].

Nanostructures are also further classified by their material combination, separating them into semiconductor–semiconductor and metal–semiconductor systems. These composites can manifest in a variety of geometries such as core/shell, [30]

dot-in-a-rod, [35–38] barbell, [39–41] heterodimer, [42, 43] tetrapod, [44] and multibranched [45] nanocrystals. Frequently utilized material combinations for metal–semiconductor systems include Au/CdSe, [46, 47] Au/CdS, [48, 49] Pt/CdS [50], and Au/PbS [22], while semiconductor–semiconductor composites often utilize II–VI or III–V materials. The following sections analyze optical properties of these systems in more detail.

This chapter provides an overview of the optical properties of the aforementioned classifications of nanocomposites throughout their synthesis. These systems have been chosen as they comprise structures that demonstrate a range of general phenomenon typical of the various types of nanocomposites currently being researched. This chapter will begin with the simpler type I system, proceeding in increasing complexity through the type II system, and terminating with the analysis of the semiconductor–metal systems. The evolution of the optical properties will be presented, along with general conclusions that can be made using the information obtained from a number of examples.

4 Experimental and Instrumental Methodology

All nanoparticle types analyzed in this chapter are fabricated using "bottom-up" methodology via solution phase colloidal chemistry. These syntheses were carried out under argon or nitrogen environment at temperatures ranging between 30 °C and 450 °C. Owing to their colloidal stability, investigated nanocomposites are usually stored in nonpolar solvents.

Steady-state UV-vis absorption and photoluminescence spectra analyzed in this chapter were recorded using UV-vis and fluorescence spectrophotometers (e.g., CARY 50 and Jobin Yvon Fluorolog). Time-resolved transient absorption spectroscopy typically employs Ti:sapphire amplified laser system operating at a repetition rate of 0.1–200 kHz, which output is split into two components: monochromatic pump and broadband probe signals. Fluorescence lifetime measurements are usually performed using a time-correlated single-photon counting setup utilizing either a single-photon counting PCI card (e.g., Becker & Hickle GmbH), or a NIM bin-based amplification system comprising a differential amplifier, constant fraction discriminator, time-to-amplitude converter, and analog-to-digital converter units. The excitation of the sample is typically performed using a picosecond diode laser, which repletion rate is chosen to allow no more than one emission photon per 5–10 excitation pulses.

5 Key Research Findings

5.1 Semiconductor-Semiconductor Nanocomposites

Conjoining multiple semiconductor domains in a single nanocomposite provides a higher degree of customization in the development of unique optoelectronic

materials. By judiciously choosing the initial domains and the geometry in which they are assembled, such heteronanocrystals can be made to offer superior control over the spatial distribution of charge carriers across material interfaces, which determines the overall functionality of the quantum system. Conventionally, a heterojunction of two semiconductor materials can be classified as either type I, where both carriers are confined within the same semiconductor, or type II, where an electron and a hole are spatially separated in two different parts of the heterostructure. Due to highly stable emissions associated with nanocrystals in the first group [51–53], their properties are readily utilized in applications that require a coupling of quantum dots to organic moieties, such as in hybrid LEDs [8, 54, 55] or in vivo imaging, [13, 56] where the use of single-phase nanocrystals typically causes an irreversible loss of fluorescence [57, 58] or severe blinking [59–61]. Heterostructures of the second group benefit from an efficient separation of charges between the core and the shell, which makes them useful in photovoltaic applications [62–66], where spatial charge separation reduces an exciton dissociation potential, or QD-based lasers [1, 67, 68], where an electric dipole of a photogenerated pair Stark-shifts the biexciton level resulting in a desirable linear light amplification regime.

One common feature, characteristic to above-mentioned carrier localization types is a straightforward correspondence between a quantum dot emission range and the energy spacing between the two closest band edges of the semiconductor materials that form the heterostructure. Indeed, for both type I and type II heteronanocrystals, the energy of emitted photons is determined by the energy difference between the closest zero-angular momentum states, 1S(e) and 1S(h), of the adjoined materials.

5.1.1 Type I Nanocomposite Systems

Type I nanosystems are constructed by combining two semiconductor materials in such a manner that conduction and valence band edges of one material fall entirely within the band gap of the other semiconductor, creating a potential barrier at the interface. Likewise, semiconductor nanocomposites comprising more than one site of attachment are referred to as type I when the higher potentials surround the low band energy semiconductor. There is also a reverse type I system where the large band energy semiconductor is located at the center of the structure and is enclosed by the lower band gap semiconductor (see Fig. 13.1). As the name suggests, the direct and reverse systems have opposite effects on the localization of excitons created within them.

In type I nanocrystals, the potential energy restriction placed on the first material by the larger band gap of the second material confines photoinduced charges to the core of the nanocomposite. Restricting charge carriers to the central semiconductor will increase the quantum efficiency of the fluorescence emission, as the lower overlap of charge carriers with the surface states of the nanocomposite causes a decrease in trapping rate. Likewise, the growth of the semiconductor shell in a type I configuration helps protecting the optical characteristics of the core domain, as in this case the photooxidation of the shell material and associated ligands does not lead to the degradation of the core component.

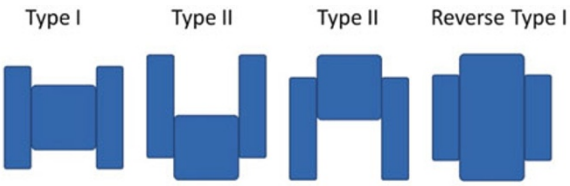

Fig. 13.1 Illustration of band-edge alignment in various system types

In reverse type I systems, the areas of lower potential energy reside on the outer edges of the heteronanocrystal such that electrons and holes are both pushed out of the central domain. In the case of a core/shell or a seeded tetrapod geometry, this would result in the injection of charge carriers from the core into the shell or arms, respectively. Reverse type I systems are less common than those with the direct type I configuration, as they generally have fewer practical uses; one known application of reverse type I systems is in LEDs which benefits from an enhanced tunability of the emission color in such nanocomposites.

CdSe/ZnSe/ZnS Core/Shell/Shell Nanocrystals

As an illustrative example of a type I nanocomposite system, CdSe/ZnSe/ZnS core/shell/shell nanocrystals will be analyzed in detail [69]. This system represents two type I systems within itself, but due to the main focus of a previous chapter on core/shell structures, the more complex core/shell/shell morphology was chosen to exemplify a broader scope of architectures.

Fabrication of CdSe/ZnSe/ZnS core/shell/shell heteronanocrystals was carried out one layer at a time, beginning with the synthesis of CdSe nanocrystals in colloidal solutions, onto which a thin ZnSe shell was then grown in a separate procedure. This step was then repeated for the growth of the ZnS shell, this time using the CdSe/ZnSe core/shell structures as seeds.

Each layer of the CdSe/ZnSe/ZnS system provides a unique aspect to the overall properties and function of the nanocomposite, with the core providing the greatest influence on the spectral character of the fluorescence. A CdSe core capped with original bulky ligands has relatively low emission quantum efficiency (typically less than 25 %) due to ligand oxidation and desorption, which promotes the interaction of the excitons with the surface states. This is mitigated by the inorganic surface passivation provided by the ZnSe and ZnS shell. The ZnSe shell is first grown to act as a transition, stress-relieve, layer between the CdSe core and the ZnS outer shell, as the lattice mismatch between the latter materials is high, roughly 12 %, and growth of ZnS directly onto CdSe would cause crystal defects, especially for shells exceeding two to three monolayers (MLs) in thickness. It should be mentioned that a sufficiently thick ZnSe shell would be able to provide adequate passivation, but ZnSe is not as stable a material and prone to photooxidation. The final ZnS shell results in comparable photoluminescence efficiencies, increased stability, and reduced biotoxicity, as ZnS is known as an innocuous material, making these nanocomposites applicable for biological labels and as well as nanocrystal LEDs.

The absorbance and emission profiles of the original CdSe cores are characteristic of binary nanocrystals exhibiting a typically sharp absorption edge and narrow

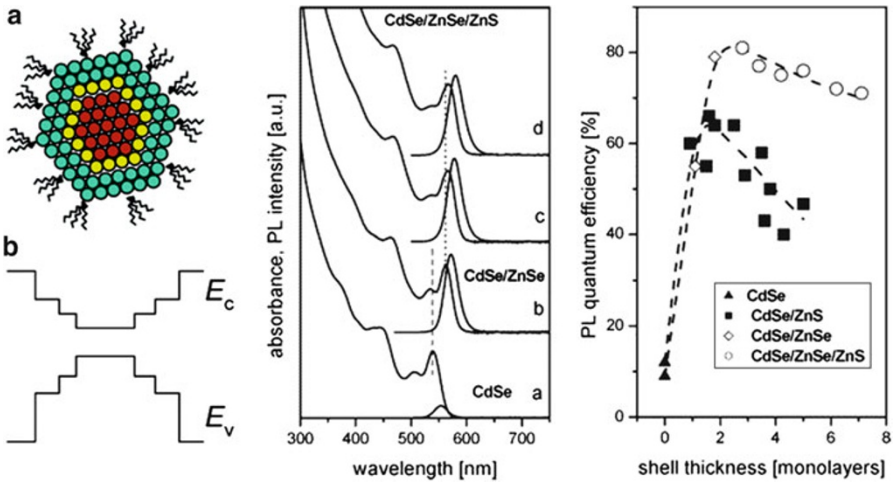

Fig. 13.2 (**a**) Schematic of core/shell/shell CdSe/ZnSe/ZnS nanocrystal. (**b**) Band gap energy diagram of CdSe/ZnSe/ZnS nanocrystal. (**c**) Absorbance and photoluminescence spectra of (a) CdSe cores, (b) CdSe/ZnSe core/shell with a two monolayer thickness for the ZnSe shell, (c) CdSe/ZnSe/ZnS core/shell/shell with a ZnS shell thickness of two monolayers, and (d) CdSe/ZnSe/ZnS core/shell/shell with a ZnS shell thickness of 4 monolayers. (**d**) Photoluminescence quantum efficiencies of various CdSe core/shell and core/shell/shell architectures depending on shell thickness (Reprinted with permission from Talapin et al. [69]. Copyright 2004 American Chemical Society)

emission width (Fig. 13.2). Growth of the ZnSe thin shell is marked by a drastic increase in photoluminescent quantum efficiency, and the associated bathochromatic (red) shift in both optical profiles due to the partial leakage of charge carrier wave packets into the shell. Upon grow minor red-shifting in both the absorbance and fluorescence occurs proportionate to the thickness of the shell as the overall volume of the nanocrystal has increased, allowing the wavefunctions to become slightly more delocalized. After the optimal thickness of the ZnS shell of roughly 2.5 monolayers is reached, the photoluminescence quantum efficiency of the ZnS layer, nanocomposites starts to decay when additional ZnS is added to the surface. The absorbance spectra show contributions from each individual structure, as is expected from multifunctional nanocrystal systems.

CdSe/CdS and CdSe/CdZnS Core/Giant Shells

Another example of a type I system is a core/shell and core/shell/shell structure that demonstrates an extreme case of charge carrier localization by implementing the growth of a giant shell around the core semiconductor [70] (Fig. 13.3). This giant shell (approximately 15–20 monolayers in thickness) not only provides means for inorganic passivation of the surface, increased stability, and increased quantum efficiency but also helps suppress nanocrystal blinking, a phenomenon best described as intermittency of fluorescence with on and off cycles lasting approximately several seconds. It is believed that nanocrystal blinking occurs when charge

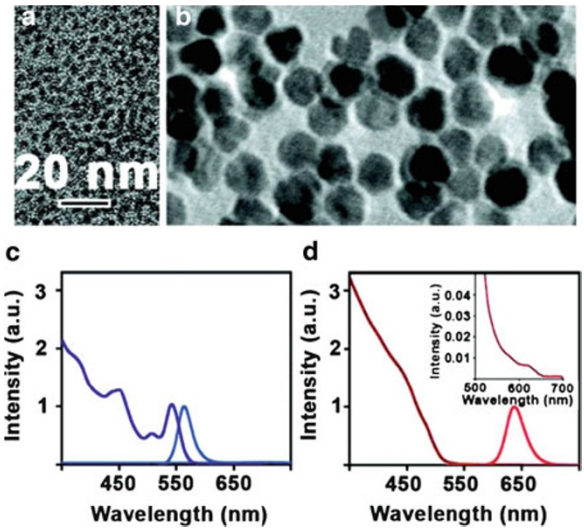

Fig. 13.3 Transmission electron microscopy (*TEM*) images for (**a**) CdSe nanocrystals and (**b**) CdSe/19CdS core/giant shells. (**c**) Absorption (*dark blue*) and PL (*light blue*) spectra for CdSe nanocrystals. (**d**) Absorption (*dark red*) and PL (*light red*) spectra for CdSe/19CdS core/giant shells (*inset*: absorption spectrum expanded to show contribution from core) (Reprinted with permission from Chen et al. [70]. Copyright 2008 American Chemical Society)

carriers get trapped on surface states whereby charging the nanocrystal, thus promoting Auger ejection or charge tunneling [59–61]. When the nanocrystal has built up charge, it will no longer fluoresce until it has regained its neutrality. Blinking must be mitigated before single nanocrystals become viable candidates for applications that require reliable single-photon emission, such as quantum informatics and biolabeling.

The synthesis of giant nanocrystals starts with the growth of CdSe seeds, 3–4 nm in diameter, then a very large shell that increases the particles diameter to 15–20 nm is fabricated by successive ion layer absorption and reaction (SILAR) [71] method. This shell can be composed of either a single material or an alloy of materials.

The absorbance profile is dominated by the shell semiconductor, as the ratio of shell to core material can reach 100:1 for nanocrystals that undergo ~20 monolayers of shell growth [70]. In the CdSe/CdS core/shell nanocrystals, this is manifested as the sharp onset of absorbance below 500 nm (Fig. 13.3d), which corresponds to the band gap of bulk CdS. Despite the presence of a thick CdS shell, which has dimensions that exceed the exciton Bohr radius for CdSe (≈ 6 nm), the emission of giant CdSe/CdS nanocrystals is dominated by the band-edge fluorescence of the core domain. This is a clear manifestation of a type I band-edge alignment, which confines photoinduced charges to CdSe. A slight increase in the wavelength of the CdSe emission upon shell growth is attributed to the minimal delocalization of charge carrier wavefunctions into the shell domain. Lastly, Fig. 13.4 shows the fluorescence intensity over time for core/shell nanocrystals, which exhibit blinking and the core/giant shell architectures, which have mitigated this intermittent fluorescence.

PbS/CdS Core/Shell Heteronanocrystals

PbS/CdS core/shell nanocomposites with the core component exceeding ≈ 3.2 nm in diameter represent another example of type I heterostructures, which show strong

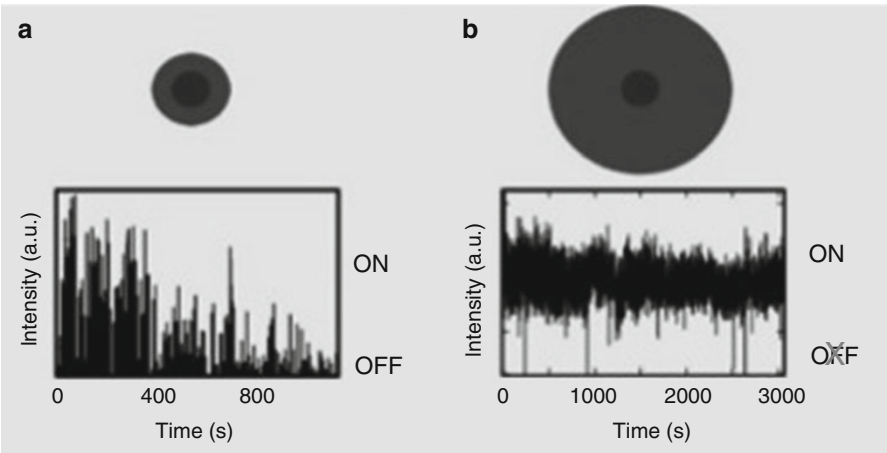

Fig. 13.4 (**a**) Fluorescence intensity over time for a blinking CdSe/CdS core/shell nanocrystal and (**b**) fluorescence intensity over time for a CdSe/CdS core/giant shell nanocrystal (Reprinted with permission from Chen et al. [70]. Copyright 2008 American Chemical Society)

band-edge fluorescence in the 1,000–2,500-nm spectral range. [72] It should be noted that PbS/CdS core/shell structures comprising smaller PbS cores (<3.2 nm in diameter) will yield type II systems due to the size tuning of the PbS 1S(e) band edge. Encapsulating larger PbS nanocrystals within a CdS shell not only enhances the emission yield of these materials but also improves the stability of the structure, which is otherwise quite susceptible to oxidation.

To initiate the synthesis, lead and sulfur precursors are reacted to create monodisperse PbS nanocrystal cores, into which a thin shell of CdS is implanted through $PbS^{2+} \rightarrow CdS^{2+}$ cation exchange. In this method, the nanocrystal cores are placed in a solution that contains an excess of Cd^{2+} cations. These Cd ions will diffuse into the outer layers of the PbS nanocrystals, replacing the Pb^{2+} and forming a thin shell of CdS. This method can be done at relatively low temperatures and slow growth conditions, allowing for the thickness of the shell to be accurately controlled. The thickness of the CdS shell can be controlled with a submonolayer precision by tuning either the temperature of the growth solution or the time of the exchange reaction [72, 73] According to the high-resolution (HR) TEM analysis of several PbS/CdS core/shell structures (Fig. 13.5), CdS shell grows uniformly on the surface of PbS nanocrystals without creating noticeable lattice defects, which is attributed to a relatively low lattice stress at the interface of PbS and CdS crystal phases (strain $\approx$ 1.7 %). A good lattice match at the core/shell boundary can also enable the growth of large CdS shells totaling 14–16 monolayers (ML).

The character of charge confinement in PbS/CdS core/shell nanocomposites is readily substantiated based on steady-state spectroscopy of excitonic transitions in these nanoparticles. According to Fig. 13.5, the $Pb^{2+} \rightarrow Cd^{2+}$ cation exchange in PbS nanocrystals results in blue-shifting of the absorption and emission features, which is attributed to the decreased length of the carrier confinement in PbS cores.

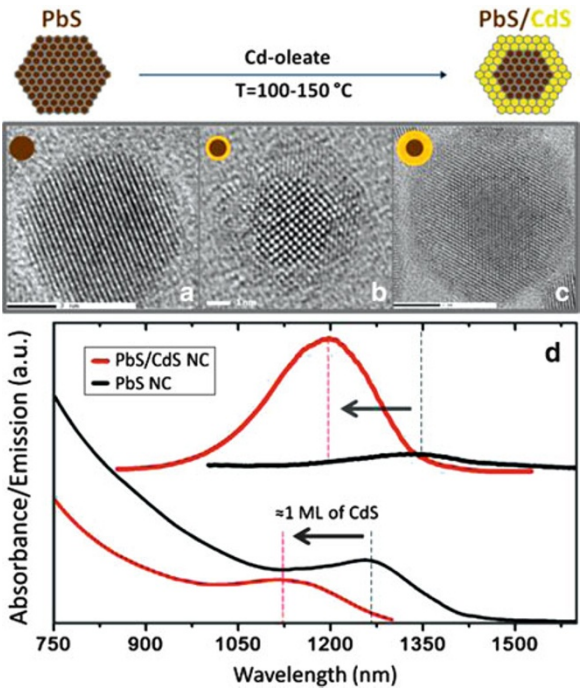

Fig. 13.5 TEM of (**a**) PbS nanocrystal, (**b**) PbS/CdS core/shell nanocrystal grown via cation exchange, (**c**) PbS/CdS core/shell nanocrystal (~15 monolayers), and (**d**) absorbance and fluorescence of PbS (*black*) and PbS/CdS (one monolayer CdS via cation exchange) (*red*) vertically offset for clarity

The magnitude of this spectral shift is proportional to the reduction in the PbS diameter and can be used here for estimating the thickness of the PbS layer that was converted into the CdS shell. In addition to blue-shifting of excitonic transitions, the transformation of PbS nanocrystals into PbS/CdS core/shell structures is accompanied by a 5–10-fold increase in the emission intensity, which reflects a diminishing probability of core-localized charges to be trapped on nanocrystal surfaces. Such enhancement of the emission yield upon shell growth is consistent with the onset of the type I carrier localization in PbS/CdS core/shell heterostructures, for which both electrons and holes reside primarily in the core domain of the composite nanocrystal.

5.1.2 Type II Nanocomposites

By choosing the sizes and materials of each domain in a heteronanostructure, a staggered alignment of the band edges at the interfaces of two materials can be achieved. This type of architecture is commonly referred to as a type II system. When an exciton is created within a type II nanostructure, the offset band gaps create a potential gradient, driving the electron and hole away from each other and spatially separating their wavefunctions. Due to a smaller degree of electron–hole overlap, type II systems generally have weaker fluorescence characteristics and longer emission lifetimes.

Type II systems will also experience a red-shift of the fluorescence peak relative to the emission of their constituents originating from the recombination taking

place at the interface between materials, whereby electrons localized in the conduction band of one semiconductor will recombine with holes residing in the valence band of the other. This type of electron–hole recombination is also known as a "spatially indirect" recombination. The typical value of a Stokes shift in type II systems is thus dependent on the magnitude of the band-edge offset and can range from just a few nanometers for CdSe/CdTe nanocrystals to hundreds of nanometers for systems such as ZnSe/CdS or ZnTe/CdS.

CdSe-Seeded CdS Nanorods and Nanotetrapods: Quasi-type II Heterostructure

Heteronanorods and tetrapods are two common morphologies of type II nanocomposites. Both structures are usually fabricated by seeding the growth of CdS or CdSe nanorods from small-diameter CdSe, ZnTe, ZnSe, or CdTe nanocrystals, where a seed nanocrystal with wurtzite lattice structure yields nanorods while seeds with a zinc blende crystal lattice promote the growth of tetrapods [69]. More generally, however, the growth of the nanorods or tetrapods morphology is controlled by a combination of the seed lattice type, seed concentration [74], reaction temperature, and ligands. For instance site-specific ligands can suppress the growth along certain axes allowing for the desired shape to be created, while the size and length of nanorods can be controlled by concentration and reaction time. Similar to previously analyzed PbS/CdS core/shells nanostructures, CdSe/CdS heterostructures can transition between type I and type II systems depending on the size of core, where larger cores will yield a type II alignment of band edges.

In the case of CdSe nanocrystals, the growth of CdS linear extensions causes notable changes in the spectroscopic characteristics. The absorbance profiles of both nanorods and tetrapods will retain the excitonic edge associated the CdSe core, which is now red-shifted, due to the increase in the confinement length of CdSe excitons, but this feature is now overshadowed by the absorbance contribution of the CdS in the linear portions of the nanorods and tetrapods, manifesting as a sharp increase in absorbance around 450–460 nm, as is characteristic of CdS. This increase will be shaped as a shoulder or ledge, rather than a peak, due to a loss in dimensionality in the confinement of CdS excitations. Increasing the size of the rods or tetrapods will have a proportional effect on the absorbance profile, as the first spectral peak will shift redder and the CdS shoulder will be increased. The absorbance contribution of CdS is significantly larger than that of CdSe due to the high volume ratio of CdS material in the linear domains to CdSe in the core. These effects can be seen in Fig. 13.7a–b, where the absorbance contribution from the CdSe core is only recognizable after significant magnification. Tetrapods also experience a larger red-shift than the nanorods, originating from the morphological effects on electronic states and an intrinsic difference in energy levels of the types of CdSe wurtzite and zinc blende crystal lattices (Fig. 13.6).

Addition of the CdS domains onto CdSe core is also reflected in the emission of the CdSe/CdS nanocomposite, which undergoes a significant increase in photoluminescence. The large absorbance cross sections of the linear components

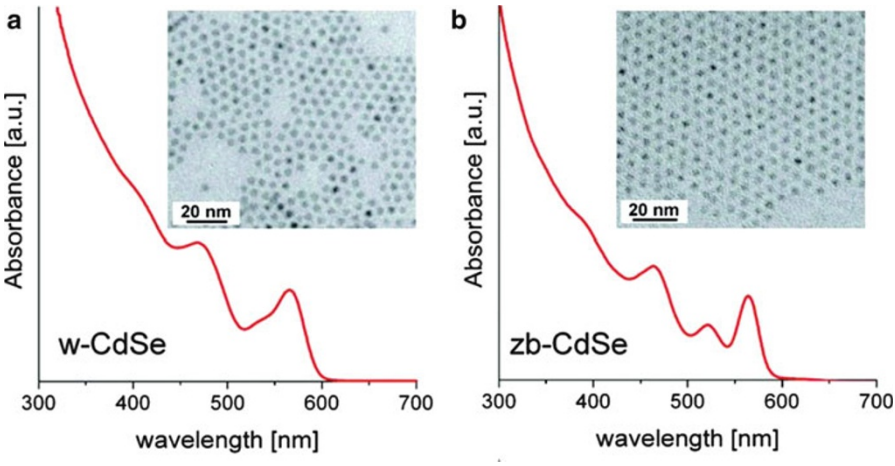

Fig. 13.6 (**a**) Absorption spectrum and TEM image of 4.4-nm CdSe nanocrystals with wurtzite lattice and (**b**) absorption spectrum and TEM image of 4.0-nm CdSe nanocrystals with zinc blende lattice (Reprinted with permission from Talapin et al. [69]. Copyright 2004 American Chemical Society)

act like antennae, increasing the number of excitons created, which will either recombine in the core (type I) or at the interface (type II). The type II fluorescence will manifest as a redder peak, as the indirect recombination is always a lower energy transition than direct recombination in either isolated semiconductor domain. Type II transitions are also accompanied by Stokes shift. In Fig. 13.7, graphs a and b, the associated Stokes shifts for nanorods and nanotetrapods are ~43 meV and ~78 meV, respectively. As the cores increase in size, this shift would become larger, due to the increasing difference in energy between the lowest absorption transition associated with CdSe and the decreasing energy of the inter-domain radiative decay.

Fluorescence lifetime also experiences a notable increase with the growth of linear extensions. Figure 13.7c and d illustrates the proportional relationship between the length of the linear structures and photoluminescent lifetimes. The trace of CdSe nanocrystals (black trace) is typical of binary nanocrystals, exhibiting nanosecond non-exponential decay. Upon the growth of rod or tetrapod "arms," the decay trend becomes nearly linear due to lower charge trapping probability, with tetrapods exhibiting lifetimes over twice as long as nanorods and nearly three times that of isolated CdSe nanocrystals.

Lastly, minor shifts in the optical spectra can be achieved by altering the dimensional parameters of the rods and tetrapods. As expected, large nanocomposites have reduced quantum confinement effects, as the carrier wavefunctions can spread out over or tunnel into a larger volume, but the spectral profiles are more sensitive to changes in dimensions that exhibit a higher degree of confinement. As a result, altering the diameter, or width, of the linear appendages initiates a more profound change than does altering the length.

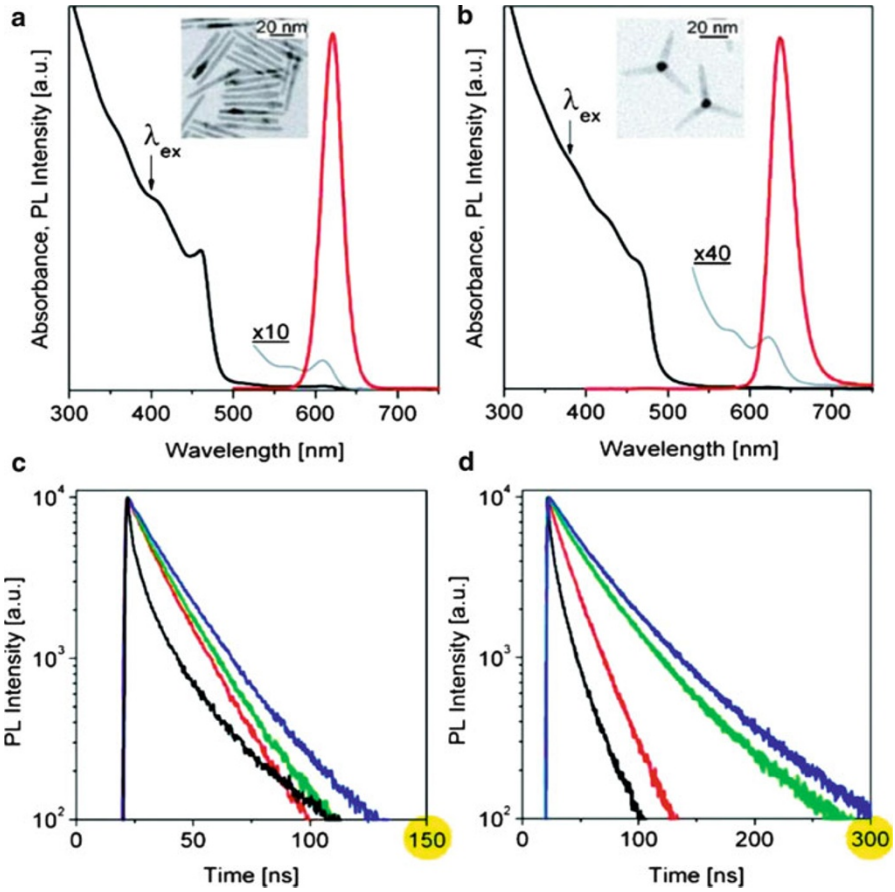

Fig. 13.7 (**a**) Absorption (*black*) and photoluminescent (*red*) spectra of 46-nm-long CdSe/CdS nanorods in toluene solution grown from 4.4-nm w-CdSe seeds. *Gray line* shows magnified absorption spectrum to elucidate the structure of the absorption onset. Absolute photoluminescent quantum efficiency of this sample was 80 %, measured at the excitation wavelength 514 nm. (**b**) Absorption (*black*) and PL (*red*) spectra of toluene solutions of CdSe/CdS nanotetrapods with 24-nm CdS legs grown from 4-nm zb-CdSe seeds. *Gray line* shows magnified absorption spectrum to emphasize structure of the absorption onset. Absolute PL quantum efficiency of this sample was 39 %, measured at the excitation wavelength 512 nm. (**c**) Fluorescence decay of 4.4-nm w-CdSe nanocrystals (*black*) and CdSe/CdS nanorods with different lengths: 12.2 nm (*red*), 24 nm (*green*), and 36 nm (*blue*). All samples were excited at 440 nm; emission was detected at the maxima of the PL spectra. (**d**) Fluorescence decay of 4.0-nm zb-CdSe nanocrystals (*black*) and CdSe/CdS nanotetrapods with arm length of 9.2 nm (*red*), 24 nm (*green*), and 38 nm (*blue*). All samples were excited at 440 nm; emission was detected at the maxima of the PL spectra (Reprinted with permission from Talapin DV, Mekis I, Götzinger S, Kornowski A, Benson O, Weller H. CdSe/ Reprinted with permission from Talapin et al. [69]. Copyright 2004 American Chemical Society.

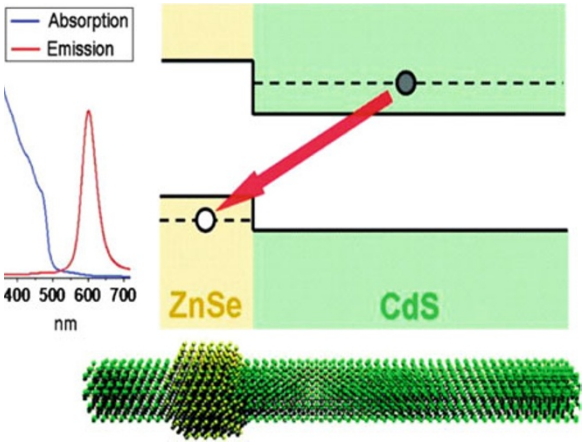

Fig. 13.8 Representation of the ZnSe/CdS type II band-edge offset and the separation of charge carriers across the interface, with electrons residing in the conduction band of CdS and holes in the valence band of ZnSe

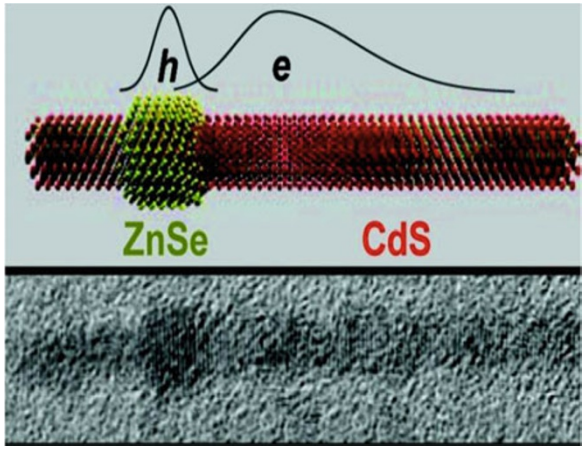

Fig. 13.9 Illustration of the domain-specific localization of electron and hole wavefunctions across the ZnSe/CdS heteronanorods (Reprinted with permission from Hewa-Kasakarage et al. [75], copyright 2009 American Chemical Society)

ZnSe/CdS (Core/Shell)-Seeded CdS Heteronanorods

ZnSe/CdS nanorods provide another example of a type II system, for which photoinduced holes are primarily localized in the ZnSe "dot" domains while electrons are delocalized along CdS "arms" (see Figs. 13.8 and 13.9) [36, 75]. These structures are fabricated in a three-step procedure, beginning with a ZnSe core, a thin shell consisting of a few monolayers of CdS, and finally a CdS nanorod "arm."

When an exciton is generated either in the core or "arm" domain of the ZnSe/CdS nanorod, the staggered band-edge alignment at the material interface leads to spatial separation of the charge carriers into different parts of the heterostructure. In spatially asymmetric nanostructures, such separation of charges could be near complete, which gives rise to unique optical properties associated with an induced electric dipole. In the case of ZnSe/CdS heteronanorods, the electron wavefunction

will spread out over the CdS domain while the hole is localized to the ZnSe component. Materials exhibiting such properties are applicable in photovoltaic technologies, where spatially separated carriers require less energy for dissociation; anisotropic light sources, where an induced electric dipole provides the capability for a high level of polarization; and optical modulators, where separation of carrier wavefunctions allows for switching of nanocrystal emission energies via quantum-confined Stark effect [75].

Figure 13.10 displays the optical properties of nanostructures after each fabrication stage involved in the synthesis of ZnSe/CdS heteronanorods. Spectral characteristics of ZnSe nanoparticles synthesized in the first reaction (Fig. 13.10a) are typical of monodisperse binary nanocrystals, recognized by a sharp absorption edge and a narrow emission bandwidth. The lingering, structureless tail, centered around 490 nm and noticeably extending into the infrared, is caused by the interaction of excitons with external media at trap states, as the surface of the nanocrystal is not optimally passivated by organic ligands at this stage. Figure 13.10, spectrum 2, demonstrates the increased contribution from trap states when the organic ligands are removed via heating, where the emission profile of unpassivated nanocrystals has lost considerable definition in its fluorescence peak.

Deposition of a thin CdS shell onto ZnSe nanocrystals results in the onset of a low-energy tail in the absorption profile (Fig. 13.10b), which extends over the visible range due to an onset of type II localization regime. This process is accompanied by quenching of type I violet emission in ZnSe nanocrystals and the appearance of a new emission feature in the visible range. This new peak originates from the radiative decay of excitons across the semiconductor heterojunction. Deep trap fluorescence associated with the original ZnSe cores can be still observed around 490 nm, as seen in Fig. 13.10d, spectrum 3, now joined by the contribution from interfacial trap states at roughly 475 nm. Together, these trap state features flank the emission peak corresponding to the spatially indirect ($1S_e$(CdS)-$1S_h$(ZnSe)) recombination in core/shell nanocrystals observed at 540 nm. As the shell increases in size, the portion of the emission spectra attributed to trap states begins to diminish (Fig. 13.10d, spectrum 4), and fluorescence lifetime continues to increase (Fig. 13.10e, trace 3).

The growth of short, 1–2-nm CdS extensions at the final stage of the synthesis leads to a near complete quenching of both deep and interfacial trap emissions, as well as continuous red-shifting of the spatially indirect fluorescence, as shown in the spectrum 5 of Fig. 13.10d. The diminishing contribution of traps to carrier relaxation for these structures is also evidenced by the increasing lifetime of the fluorescence intensity decay (Fig. 13.10e, trace 5).

Optical characteristics of high-aspect-ratio (ZnSe/CdS)/CdS heteronanorods are shown in Fig. 13.10c. Due to the delocalization of electronic wavefunctions into the increased volume of CdS, the emission of $\approx$ 100-nm heteronanorods undergoes a 10–15-nm red-shift from the peak position in short-branched (ZnSe/CdS)/CdS heterostructures (Fig. 13.10d, spectrum 5). Growth of linear CdS extensions is also accompanied by the 10–20-nm decrease in the spectral width of the emission, which is consistent with further quenching of trap state emission as well as the

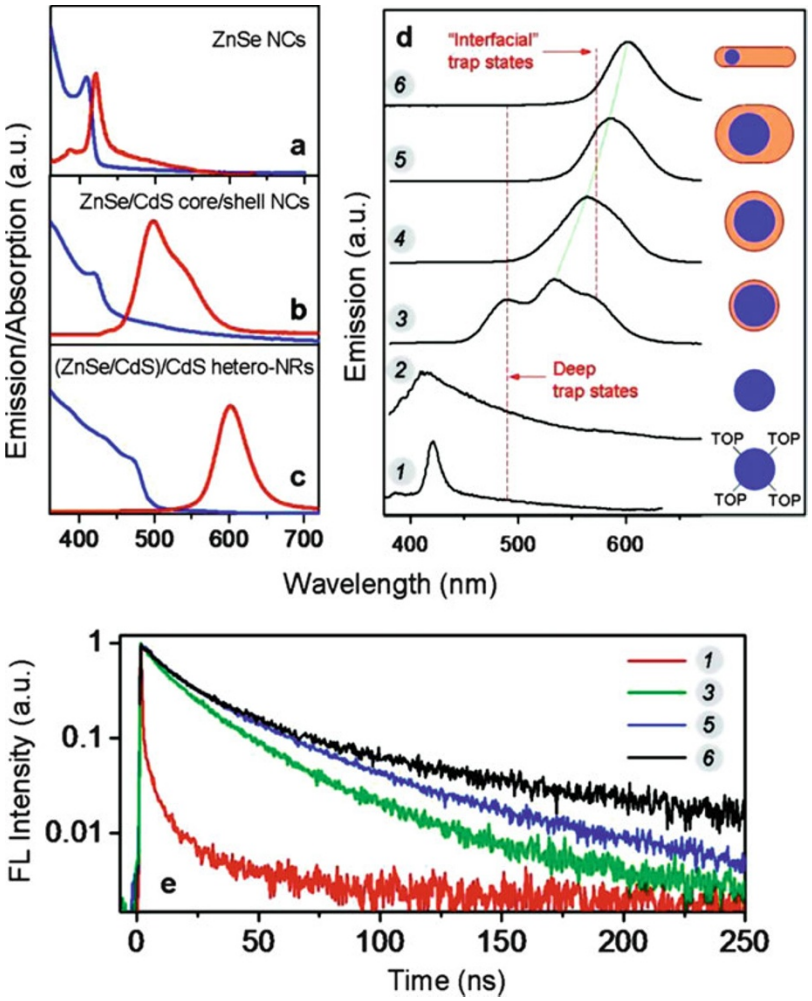

Fig. 13.10 Optical characteristics of nanocrystal and nanorod colloids. UV-vis absorption and steady-state fluorescence spectra for (**a**) 5-nm-diameter ZnSe nanocrystals; (**b**) ZnSe/CdS core/shell nanocrystals, fabricated by depositing teo to three monolayers of CdS; and (**c**) high-aspect ratio (ZnSe/CdS)/CdS heteronanorods. (**d**) Evolution of the fluorescence spectra during the three-stage synthesis, showing the trap state emission. Deep traps contribute to the emission near 490 nm as evidenced by the broad emission tail in passivated (spectrum 1) and unpassivated (spectrum 2) ZnSe nanocrystals. ZnSe/CdS core/shell nanocrystals with ca. 1 monolayer of CdS exhibit both deep and interfacial trap emission (spectrum 3). The former becomes quenched in thick-shell ZnSe/CdS nanocrystals (spectrum 4), while the latter is reduced in large-size (oblong) core/shell structures (spectrum 5) and becomes fully quenched in long (ZnSe/CdS)/CdS heteronanorods (spectrum 6). (**e**) Fluorescence intensity decay for ZnSe (*red*), thin-shell ZnSe/CdS nanocrystals (*green*), thick-shell ZnSe/CdS nanocrystals (*blue*), and (ZnSe/CdS)/CdS heteronanorods (black), measured by means of TCSPC technique (Reprinted with permission from Hewa-Kasakarage et al. [75]. Copyright 2009 American Chemical Society)

increase of CdS shell beyond the "saturation" value associated with the onset of type II localization regime.

The fluorescence intensity decay of (ZnSe/CdS)/CdS heteronanorods is shown in Fig. 13.10e, trace 6. It is expected that radiative relaxation of spatially separated excitons may exhibit unique relaxation times that arise from intrinsically different carrier decay mechanisms associated with a weak-confinement regime. Owing to a nonzero quantum yield and spatial separation of charges, fabricated heteronanorods provide a model system for testing such hypothesis. According to traces 5 and 6 in Fig. 13.10e, both short- and long-branched nanorods exhibit non-exponential radiative relaxation of excited carriers, which is usually expected of semiconductor quantum systems due to mixing of contributions from different single-exponential lifetimes corresponding to "on" and "off" blinking cycles [76]. The fluorescence lifetime of high-aspect-ratio heteronanorods appears to be longer than in short-branched heterostructures (Fig. 13.10e, traces 5 and 6), possibly the result of fewer carrier traps present at the ZnSe/CdS interface or smaller overlap between electron and hole wavefunctions brought by the delocalization of electrons in CdS. The overall character of carrier relaxation in high-aspect-ratio heteronanorods, however, appears to be similar to that of short heteronanorods or even core/shell nanocrystals, indicating that a mechanism of radiative recombination across the ZnSe/CdS heterojunction is majorly independent of the degree of charge separation.

ZnSe/CdS/ZnSe Nanobarbells and Transient Absorption Spectroscopy

In this section, we probe further into the optical properties of type II heterostructures by reviewing the time-dependent changes in the absorption spectra of ZnSe/CdS nanocomposites. To this end, the femtosecond transient absorption (TA) spectroscopy is employed to provide a more detailed picture of the ultrafast carrier dynamics in a barbell-like arrangement of ZnSe spheres and CdS nanorods [77]. In these experiments, excited state populations for both ZnSe and CdS materials were obtained through careful evaluation of measurements of the Stark effect and state-filling contributions into observed bleach recovery traces. It is reported that selective excitation of ZnSe tips results in an ultrafast transfer ($<$0.35 ps) of excited carriers into CdS domains, whereas resonant pumping of CdS portions of barbells leads to a comparatively slow injection of photoinduced holes into ZnSe domains ($\tau_h = 95$ ps). The observed interfacial electron transfer occurring under resonant pumping conditions is faster than CdSe/CdTe [26] and CdSe/CdS [27] heterostructures, regardless of the large spatial delocalization of corresponding wavefunctions across the ZnSe/CdS nanocomposite. This phenomenon, attributed to the near-epitaxial relationship between ZnSe and CdS crystalline domains, is expected due to a relatively small lattice mismatch (2.7 %) between junctioned lattices that reduces interfacial strain, thus lowering the occurrence interfacial defects.

Together, the fast spatial separation of photoinduced charges along the main axis of ZnSe/CdS barbell and the availability of both carriers for a chemical reaction with external media can be utilized for a number of optoelectronic applications.

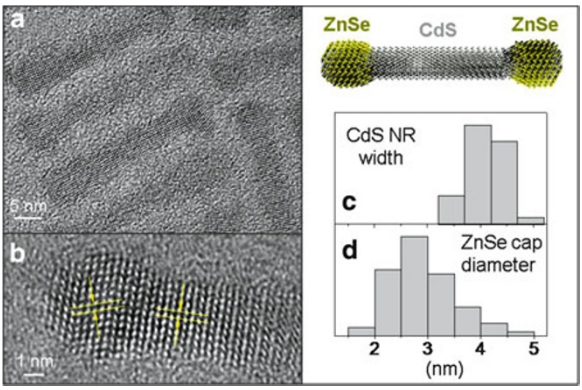

Fig. 13.11 Structural analysis of ZnSe/CdS barbells. (**a**) High-resolution transmission electron microscope (*TEM*) images of ZnSe/CdS heterostructures. (**b**) A typical ZnSe/CdS barbell showing unique directions of lattice planes for each of the material domains. (**c**) Statistical distributions of barbell widths and diameters of ZnSe tips (in (**d**)) (Reprinted with permission from Hewa-Kasakarage et al. [148]. Copyright 2010 American Chemical Society)

For instance, ZnSe/CdS is particularly well suited as a component for nanocomposites capable of photocatalytic water splitting since the electrochemical potentials of electrons and holes in ZnSe/CdS barbells straddle the H_2/H_2O and O_2/H_2O redox potentials [77, 78]. In addition, fast charge transfer between ZnSe and CdS domains can be harnessed in applications that rely on photoinduced electric dipoles to modulate the spectral response of the material, such as electroabsorption switching and modulation [79], as is also demonstrated in ZnSe/CdS nanorods exhibiting a photoinduced shift of the emission wavelength due to the quantum-confined Stark effect [75]. In the case of ZnSe/CdS barbells, the observed sub-picosecond electron transfer can enable switching rates of up to 1–2 THz, which exceed the present day characteristics of Ge-based electroabsorption modulators by an order of a magnitude [80].

Motion of excitons in the ZnSe and CdS domains of a barbell structure is confined in three and two dimensions, respectively, with a corresponding degree of confinement determined primarily by the size of ZnSe tips and widths of CdS nanorods. Accurate determination of these geometric parameters prior to spectroscopic characterization of the system is thus critical for establishing expected carrier energies in both materials. Average sizes of ZnSe and CdS domains are calculated using data from high-resolution (HR) transmission electron microscopy (TEM) measurements. Figure 13.11a and b displays typical HR-TEM images of several ZnSe/CdS heterostructures, where the barbell-like arrangement of materials can be identified by the characteristic direction of lattice planes in ZnSe tips compared to those in the CdS nanorods. Statistical analysis of approximately one hundred of such barbells shows a 5.7-nm increase of length along the 001 axis in comparison with the CdS nanorods used for seeding the growth of ZnSe, and the average tip size is 2.89 nm while the average width of barbells is roughly 4.1 nm.

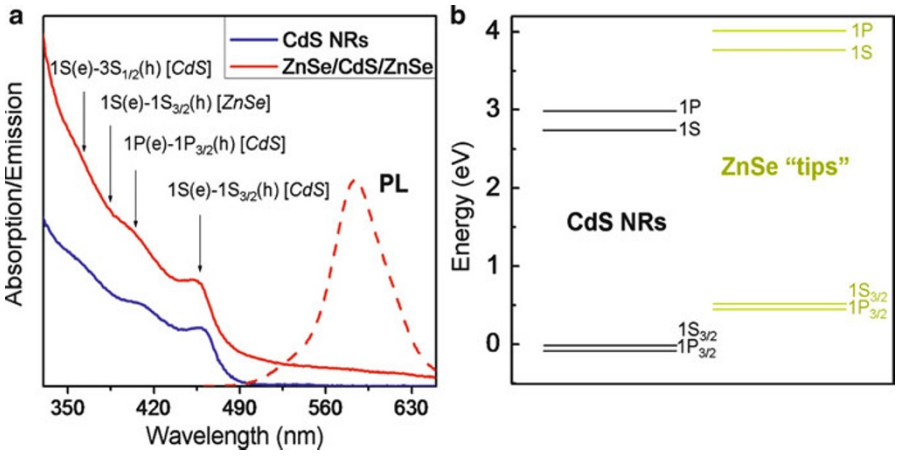

Fig. 13.12 Determination of excited state energies in ZnSe/CdS heterostructures. (**a**) Steady-state absorption and emission ($\lambda_{excitation} = 420$ nm) spectra of ZnSe/CdS barbells (*red*) and CdS nanorods (*blue*). Four lowest energy excited state transitions are identified in the absorption spectra. (**b**) Calculated excited state energies for ZnSe/CdS heterostructures comprising 4.1-nm-wide CdS nanorods and 2.85-nm ZnSe tips (Reprinted with permission from Hewa-Kasakarage et al. [148], copyright 2010 American Chemical Society)

Steady-state absorption measurements confirm the narrow distribution of barbell widths, inferred from the well-pronounced excitonic features related to the 1S(e)-$1S_{3/2}$(h) and 1P(e)-$1P_{3/2}$(h) transitions in CdS (Fig. 13.12a). The band-edge absorption in the ZnSe portion of barbells, which spectral position is expected to peak [81] at 384 nm, is not recognizable in this profile possibly due to the relatively small composition of ZnSe in the overall volume of the nanocomposite, though evidence of carrier absorption across the band gap of ZnSe is still provided by the observable change in the slope of the absorption curve below 380 nm and the apparent bleaching of the band-edge transition in time-resolved transient absorption measurements (Fig. 13.13c).

The relative alignment of $n = 1$ excited state energies in each component of the ZnSe/CdS heterostructure is shown in Fig. 13.12b. Excited electrons find the minimum of the conduction band in the 1S(e) state of CdS nanorods, which is positioned 0.80 eV lower than the 1S(e) energy of ZnSe tips. Meanwhile, photoinduced holes will localize in the $1S_{3/2}$(h) level of the ZnSe domain, which lies 0.53 eV above the valence band edge of CdS nanorods. As expected, the energy of the spatially indirect transition associated with the decay of carriers across the ZnSe/CdS interface is lower than the band gap of either ZnSe or CdS materials, accounting for the red-shifted emission of ZnSe/CdS heterostructures ($\hbar\omega = 2.1$ eV), as seen in Fig. 13.12a.

The photoinduced filling of excited states in nanocrystals leads to bleaching of interband optical transitions, such that absorption changes are proportional to the number of excited carriers:

$$\Delta A(\hbar\omega) = -\sum_i A_{0,i}(\hbar\omega - \hbar\omega_i)(n_i^e + n_i^h) \tag{13.1}$$

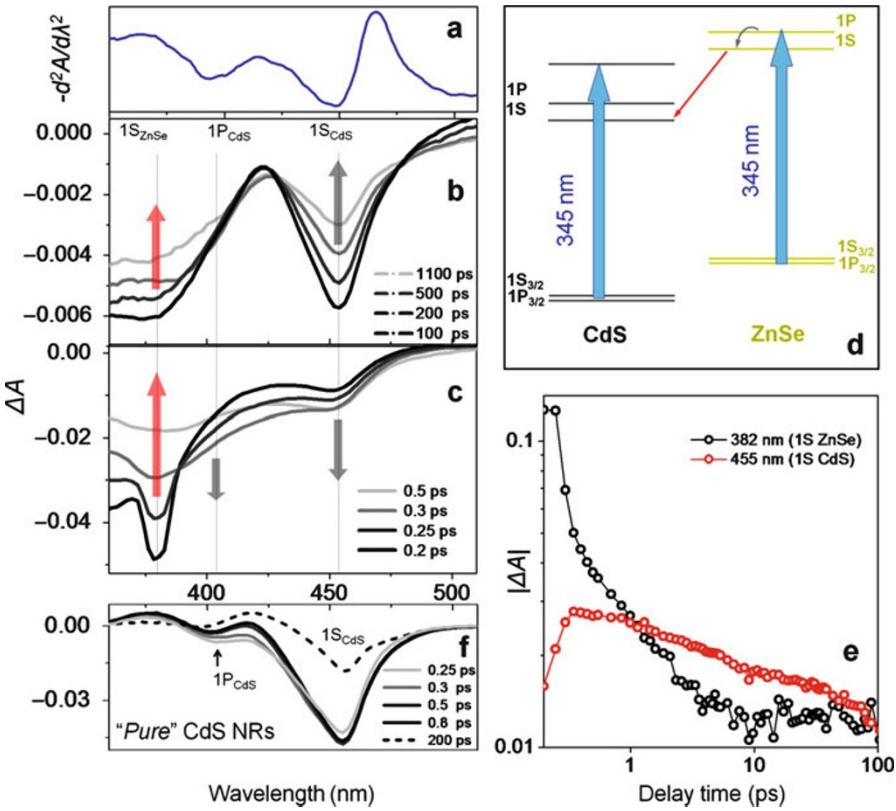

Fig. 13.13 Transient absorption measurements of ZnSe/CdS barbells resulting from resonant excitation of ZnSe domains ($\lambda_{pump} = 345$ nm). (**a**) Second derivative of the absorption profile. (**b**) and (**c**) Transient absorption spectra, $\Delta A = A(\text{pump + probe})\text{-}A(\text{probe})$, corresponding to long (**b**) and short (**c**) delay times. (**d**) Energy diagram of electronic states showing the maximum energy of pump photons (*blue arrows*) under resonant excitation of ZnSe domains. (**e**). Temporal dynamics of the transient absorption bleach recovery measured for band-edge excitons in CdS (*red*) and ZnSe (*black*) materials. (**f**). Transient absorption spectra of pure CdS nanorods ($\lambda_{pump} = 345$ nm) (Reprinted with permission from Hewa-Kasakarage et al. [148]. Copyright 2010 American Chemical Society)

where $A_{0,i}$ is an absorption profile of the ith transition and n_i^e and n_i^h are occupation numbers of electron and hole states involved in the transition. Since the effective masses of holes in CdS and ZnSe materials are approximately four to five times greater than those of electrons, their room-temperature occupation probabilities are small. As a result, the state-filling-induced absorption changes are dominated by electrons [82]. The contribution of holes into bleaching is further reduced due to exchange interaction that splits the 1S exciton into two different hole states, [83, 84]

such that the higher energy absorption transition states stay unoccupied until the lower energy hole state is completely filled, which occurs only when $\langle N \rangle >> 1$.

Another possible contribution into bleaching of nanocrystal optical transitions is due to local fields that alter transient spectra via Stark effect [85]. This leads to a spectral shift of absorbing transitions as well as changes in the corresponding oscillation strengths resulting from modifications in selection rules. In systems that produce a spatial separation of charges, such as the barbell nanostructures investigated here and type II systems in general, the contribution of the Stark effect can be particularly significant and its evaluation is necessary to properly assess the state-filling dynamics. As a semi-empirical approach to predicting the spectral changes in the transient absorption spectra of ZnSe/CdS barbells resulting from the Stark effect, a formalism [86, 87] is implemented that relates the effect of carrier-induced local fields in semiconductor nanocrystals with a repulsion between proximal transitions, such that the Stark effect contribution into ΔA can be modeled by the second derivative of the absorption profile.

The transient absorption spectroscopy of hexane-suspended ZnSe/CdS barbells is analyzed using two excitation regimes that correspond to the resonant pumping of the $n = 1$ transitions in CdS and ZnSe domains of the structure. Transient absorption spectra resulting from the quasi-resonant excitation of ZnSe tips are analyzed in Fig. 13.14. The wavelength of the pump beam, in this case, was set to 345 nm, which allows excitation across the two lowest energy transitions in the ZnSe domain: 1S(e)-$1S_{3/2}$(h) and 1P(e)-$1P_{3/2}$(h), denoted as $1S_{ZnSe}$ and $1P_{ZnSe}$, respectively, as well as three lowest transitions in CdS nanorods: 1S(e)-$1S_{3/2}$(h), 1P(e)-$1P_{3/2}$(h), and 1S(e)-$3S_{1/2}$(h), as shown in the energy diagram (Fig. 13.14d). Bleaching of band-edge transitions in both materials was observed as quickly as 200 fs after excitation (Fig. 13.14c) with spectral positions of bleach signals near the expected energies of $1S_{ZnSe}$ and $1S_{CdS}$ excitons (Fig. 13.13).

The modification of the bleach signals in the transient absorption induced by the Stark effect is estimated by comparing the second derivative of the absorption spectra (Fig. 13.14a) with the short-time transient spectra (Fig. 13.14c), revealing what initially seems to be a similarity in corresponding slopes both in the case of CdS (450–465 nm) and ZnSe (385–405 nm) transitions. However, if the short-time bleach has a significant contribution from the local fields, then the two maxima of d^2A/dt^2 would coincide with the photoinduced absorption ($\Delta A > 0$) in the transient absorption spectra, which is not observed here, as ΔA remains negative throughout the entire spectral window of the probe beam. Furthermore, the initial modification of transition energies attributed to the Stark effect typically diminishes within a few picoseconds, causing a noticeable shift of the bleach minima, yet spectral positions of $1S_{CdS}$ (450–465 nm) and $1S_{ZnSe}$ (370–395 nm) transitions are nearly constant within the entire nanosecond delay range (Fig. 13.14b). Based upon these observations, it is concluded that the influence of the Stark effect on transient absorption spectra for this nanocomposite is negligible, and the observed transient absorption bleach is attributed primarily to state filling in ZnSe and CdS domains.

Selective excitation of carriers into the CdS domain of ZnSe/CdS barbells is performed using 420-nm pump pulses, for which photon energies fall below the

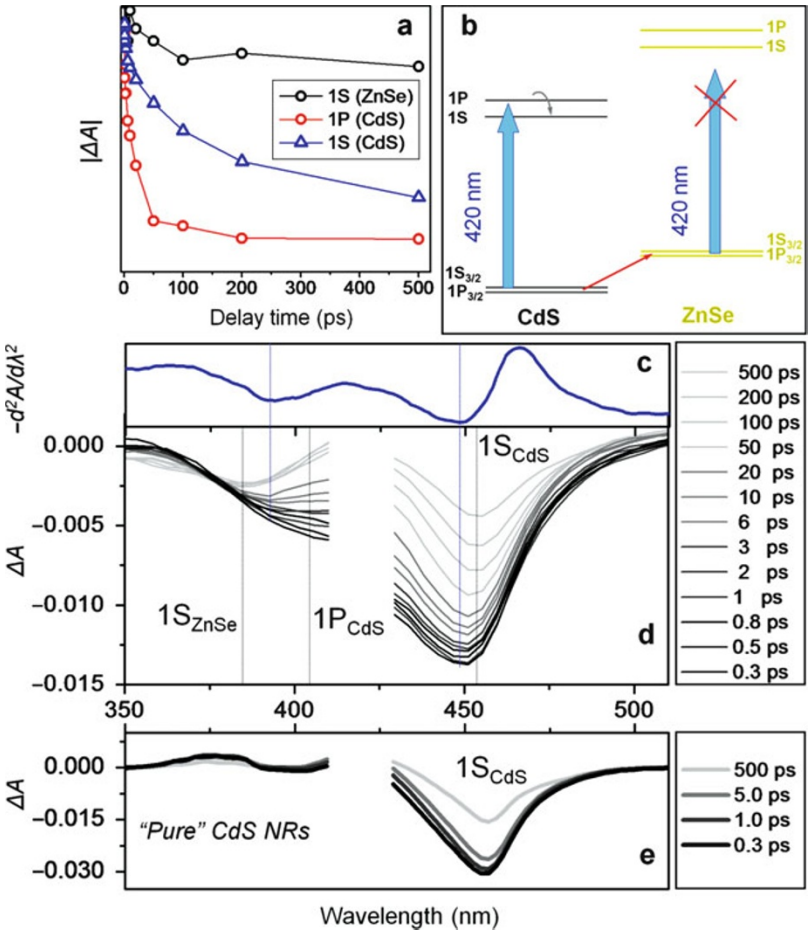

Fig. 13.14 Transient absorption measurements of ZnSe/CdS barbells resulting from selective excitation of CdS domains ($\lambda_{pump} = 420$ nm). (**a**) Temporal dynamics of the transient absorption bleach recovery for 1S(e)-$1S_{3/2}$(h) excitons in ZnSe (*black*), 1P(e)-$1P_{3/2}$(h) excitons in CdS (*red*), and 1S(e)-$1S_{3/2}$(h) excitons in CdS (*blue*). (**b**). Energy diagram of electronic states showing the maximum energy of pump photons (*blue arrows*) under selective excitation of CdS domains. Note that the average photon energy is not sufficient to induce absorption in ZnSe. (**c**) Second derivative of the absorption profile. (**d**) Transient absorption spectra of ZnSe/CdS barbells resulting from $\lambda_{pump} = 420$ nm excitation pulses. (**e**) Transient absorption spectra of pure CdS nanorods ($\lambda_{pump} = 420$ nm) (Reprinted with permission from Hewa-Kasakarage et al. [148], copyright 2010 American Chemical Society)

band gap of ZnSe tips. According to the energy diagram in Fig. 13.14b, these photons can only be absorbed through the excitation of 1S and 1P excitonic transitions in CdS nanorods, while excited states of the ZnSe component remain essentially unoccupied. Experimental evidence of the selective carrier injection into CdS portion of barbells is seen in the transient absorption spectra, where the

early-time bleach occurs primarily in the spectral range of the lower energy $1S_{CdS}$ transition. In addition to strong optical bleaching in CdS, a weak negative signal was also observed in the wavelength range of the $1S_{ZnSe}$ transition, which is energetically positioned 0.3 eV above those of excitation photons (Fig. 13.14d). Such above-the-threshold bleaching was attributed to the energy-independent effect of local fields (Stark effect) and not the state filling, as can be inferred by nearly identical behavior of the short-time transient absorption curve and the second derivative of the absorption profile (Fig. 13.14c). For instance, the effect of local fields on $1S_{ZnSe}$ and $1S_{CdS}$ bleaching signals can be easily identified in early time traces ($\Delta t < 1$ ps) as spectral shifts of both peaks by several nanometers from their longer-delay position ($\Delta t > 100$ ps), as indicated by the offsets of blue and gray lines in Fig. 13.14d. A sizable contribution of Stark effect into transient absorption is also identified by the remarkable similarity between ΔA ($\Delta t < 1$ ps) and $d^2A/d\lambda^2$ slopes throughout the most of the spectral range. Therefore, experimental TA data provides strong evidence for photoinduced charge transfer between the ZnSe and CdS nanocrystalline domains, which can be controllably performed in either direction by modulating the excitation wavelength, such that the resonant excitation of carriers in the ZnSe material leads to 350-fs injection of electrons into CdS, and the excitation of carriers in the CdS portion of barbells results in a slower transfer of holes into ZnSe.

5.2 Semiconductor-Metal Nanocomposites

Bulk heterojunctions of metal and semiconductor materials have long been of interest to fundamental science and device engineering due to the unique interaction of respective domains through the formation of the space-charge region, [88] which gives rise to numerous technological applications including Schottky barrier solar cells, solid-state lasers [89], light-emitting diodes [90], and field-effect transistors [91]. Recent progress in synthetic methodology of nanocomposite fabrication has extended the utility of metal–semiconductor heterojunctions to the nano realm, which has given rise to new opportunities for designing multifunctional materials with properties that cannot be obtained in the bulk phase. These hybrid nanocrystals attribute their properties not only to the size, shape, and configuration of the structure as a whole but also to the unique interaction of excitons in semiconductor materials and the characteristic surface plasmon resonance effect of the metal nanoparticles. These synergistic effects allow the nanostructures to function in ways well beyond their bulk and isolated individual forms [31, 46, 92–98]. Owing to these advances, a wide array of nanocomposite morphologies, including metal-core/semiconductor-shell heterostructures, [42, 99, 100] metal-tipped semiconductor nanocrystals (NCs), [46, 49, 101–107] and organically and non-epitaxially [99, 108, 109] coupled metal–semiconductor composites have been proposed in the past decade for manipulating energy at the nanoscale with potential application of these nanomaterials in areas of photovoltaics and solar fuel production, [110] lasers, [111] and Schottky detectors [112]. Other possible applications of

metal–semiconductor nanocomposites also include nanoscale wiring. For instance, semiconductor domains decorated with metal tips on both sides have been proposed for use as electrical interconnects in nanoscale circuitry [113], while semiconductors capped with a metal domain on one side can be harnessed as a charge separating unit in photovoltaic [114], or photocatalytic [74] composites.

Of a particular interest is a fundamental interaction between semiconductor excitons and surface plasmons of metal nanoparticles, which results from the modification of the exciton dipole moment due to local electromagnetic modes of surface plasmon [115, 116]. This interaction is enabled by the nanoscopic nature of both material domains and has a unique effect on optoelectronic properties of a composite metal–semiconductor system, which has been shown to dramatically alter the energy flow that occurs across metal–semiconductor junctions. Plasmon resonance is an energetic effect arising from oscillations of conduction electrons in metal nanoparticles due to interaction with the undulating electric field of light. As the frequency of light approaches a resonant value, the amount of light absorbed by the metal nanoparticle increases along with the amplitude of the electron oscillations, until the maximum magnitude is reached at the resonance frequency. The latter depends both on the size and composition of the metal nanoparticle as well as the dielectric constant of the surrounding medium. The surface plasmons of the metal domain interact with the excitons of the semiconductor by modifying the dipole moment of the exciton with its short-range electromagnetic modes [99, 115]. This interaction dramatically changes the flow of energy across the metal–semiconductor interface, which in turn alters the optoelectronic properties of the nanostructure. As an example, the generation of a plasmon radiative field in metals, caused by resonant oscillations of low-energy conduction electrons, can strongly influence the dynamics of excitons in conjoined semiconductor nanocrystals via two unique interaction mechanisms: plasmon–exciton energy transfer and modification of the local radiation field in semiconductor domains.

Exciton–plasmon interactions in the weak coupling regime are characterized by the presence of a substantial potential barrier at the interface of semiconductor and metal components and are achieved by implementing spacer molecules for non-epitaxial domain coupling. For these composites, the emission intensity in semiconductor domains may undergo an increase [117–124] due to the plasmon-induced enhancement of semiconductor radiative rates, [125, 126] an effect that shows promise in improving the process of light amplification in lasers [90, 127–130]. Likewise, the plasmon-induced enhancement of the electric field in semiconductor domains has been documented to increase the absorption cross section of semiconductor nanocrystals, [131, 132] thus promoting the development of light-concentrating nanocomposites in an effort to aid the energy harvesting mechanism in photovoltaic and photocatalytic applications [110, 132]. In addition to intensity enhancement, spectral modification of the semiconductor emission in semiconductor–metal composites has also been utilized for sensing target proteins attached to the linker moiety in Au/CdTe assemblies [133]. Finally, a weak exciton–plasmon interaction achieved through non-epitaxial coupling of metal and semiconductor domains using a core/shell morphology has been employed for controlling the spin

of Au nanoparticles [108], with a potential application of this phenomenon in quantum information and spintronics [134–136].

A particularly strong coupling between plasmons and excitons can be realized when metal and semiconductor domains are coupled directly, without spacing moiety in-between. The potential barrier between adjacent materials in this case becomes sufficiently small to allow inter-domain charge transfer, as well as a mixing of electronic states at the metal–semiconductor interface. Additionally, the enhanced electromagnetic field attributed to the metal plasmons in a strong coupling mode may procure further modifications to the carrier dynamics associated with shared oscillations of the excitation energy between the metal and semiconductor domains. This strong coupling interaction with the shared oscillations is known as Rabi oscillations [137]. Electronic interactions such as these alter the overall optoelectronic properties of hybrid nanocomposites, imparting the structure as a whole with significantly different effects and function than its isolated parts and giving metal–semiconductor hybrid systems a more diverse assortment of spectroscopic and emission characteristics than their previously analyzed semiconductor–semiconductor counterparts.

The spatial proximity of semiconductor and metal domains (so-called strong coupling regime) can significantly alter the optical characteristics displayed by the nanocomposite. For instance, the fluorescence of the semiconductor domain can either undergo suppression [138], which is the case in many directly coupled systems; enhancement [139], which commonly occurs when the two domains are separated by a spacer; or a partial suppression. The fluorescence quenching in metal–semiconductor nanocomposites can be attributed to the transfer of the exciton energy into the metal domain via FRET mechanism. Another possible reason for the suppression of fluorescence in metal–semiconductor composites is the ultrafast transfer of photoinduced charges from semiconductor nanocrystals to a metal. This type of nonradiative decay is common in materials such as Ag/ZnO and Au/CdS tipped nanorods or Au/PbS and Au/PbSe hybrid dimers and core/shell morphologies.

Fluorescence enhancement is observed less often than a complete nullification of emission, as these effects require more complicated architectures to be created [139]. Ordinarily, enhancement is observed when the metal–semiconductor domains are within close spatial proximity of each other while separated by a large potential barrier, effectively increasing the absorbance cross section without opening up nonradiative decay pathways, as seen in systems of Au nanoparticles chemically linked to CdTe nanowires [109]. Intermediate effects occur when precise morphological conditions are met, so the energy of the plasmons can instead be partially transferred to the semiconductor domain. For example, CdS nanorods conjoined with Au nanoparticles are known to completely quench the fluorescence, while Au nanocrystals with partial CdS shells grown over the core yield an intermediate enhancement.

The absorbance profile of the semiconductor nanocrystal component can likewise undergo significant changes upon coupling of the metal domain. The excitonic features of the semiconductor may experience broaderning [34, 139] rendering

the structural features of its spectrum less defined. While the individual contributions of each structural domain still greatly influences the shape of the spectrum, the overall spectral characteristics of metal–semiconductor nanocomposites are typically a nonlinear combination of its separate parts. This is reasoned to arise from mixing of electronic states between the two dissimilar materials, which modifies the density of states and alters the absorbance profile. It has also been observed that the degree in which the spectroscopic properties of a semiconductor are changed is strongly dependent on the size and number of metal domains.

5.2.1 CdS/Au Nanocomposites

Recently, Au/CdS and Au/CdSe heterostructures comprising gold domains grown onto cadmium chalcogenide semiconductor nanorods have emerged as a model system for studying the properties of metal–semiconductor nanocomposites [49, 101, 103, 104, 107]. Besides being a system of choice for advancing synthetic protocols and investigating plasmon–exciton interactions, these nanocomposites have been considered for applications in areas of solution-processed solar cells [140, 141] and nanoscale wiring [113]. For instance, it was demonstrated that CdSe nanorods capped with gold on both ends lead to a 10^5-fold increase in carrier conductivity as compared to pristine CdSe nanorods placed over metal contacts [113], which exemplifies the potential of these heterostructures as nanoscale electrical interconnects. On the other hand, CdS nanorods capped with gold at a single end can be harnessed as charge-separating units in photocatalytic and photovoltaic devices [114].

The effect of metal domains on the properties of semiconductor counterparts is best illustrated through the evolution of the absorption features during the synthesis of metal–semiconductor nanocomposites. The growth of small-diameter metal domains onto nanocrystals or nanorods is typically performed via reduction of $AuCl_3$ salts in a mixture of toluene, dodecyldimethylammonium bromide (DDAB), and dodecylamine (DDA) [46]. To promote the growth of large-size metal tips, either light-[104] or thermal-assisted [106] methods can be used. The latter approach relies on temperature controlled reduction of $AuCl_3$ on the surface of semiconductor nanorods in the presence of oleylamine. At roughly 60 °C, the threshold energy is reached for nucleation of Au particles, which initiate growth by attaching an ion to the semiconductor at defects in the crystal lattice. This creates a nucleation site allowing additional ions aggregate, eventually forming composite structures comprising small metal tips either ends with clusters of gold nucleated along the length of the rod (Fig. 13.17a). As the temperature is slowly increased, it becomes energetically unfavorable for the gold aggregates to remain along the linear semiconductor domain, and they begin to redissolve into solution. Through this process of Oswald ripening, the gold is transferred strictly to either end of the nanorod. Further controlled increase of the temperature continues to alter the energetics, now rendering the asymmetric forms of the nanocomposite.

The absorbance profile of metal–semiconductor nanocomposites comprising CdS nanorods coupled to Au domains grown via the aforementioned thermal-assisted approach is shown in Fig. 13.15. The spatial confinement of optical

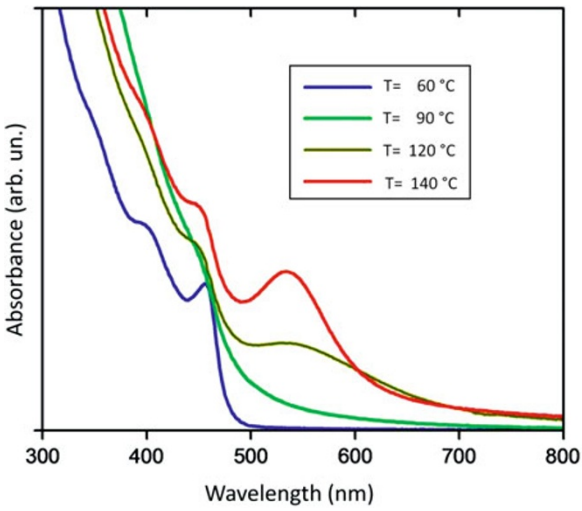

Fig. 13.15 Absorbance of Au/CdS nanocomposites of temperature-dependent morphologies (Reprinted with permission from Khon et al. [106]. Copyright 2010 American Chemical Society)

excitations in the transverse direction of CdS rods gives rise to a characteristic excitonic edge around 465 nm, which corresponds to the lowest energy transition, $1S(e)\text{-}1S_{3/2}(h)$, in these nanostructures [142]. The sharpness of the absorption edge in Fig. 13.15 confirms a narrow dispersion of nanorod widths, which agrees well with corresponding statistical distribution obtained from TEM images of these structures (Fig. 13.16a). The absorption spectra of isolated Au nanoparticles are examined in Fig. 13.18a. Since the excitation of surface plasmons in metals is a resonant process, its frequency is dependent on the composition, size, and shape of metal nanoparticles, as well as their dielectric environment. Changes in optical properties of Au/CdS nanocomposites during the growth of Au domains are summarized in Fig. 13.15. At $T = 90\ ^\circ C$, the absorption profile of Au/CdS nanoparticles exhibits noticeable changes from that of pure CdS nanorods, with the main difference occurring in the wavelength range above $\lambda = 550$ nm, where the absorption of heterostructures is increased. This red tail is attributed to the contribution from interfacial trap states as well as to optical transitions in small-size gold clusters forming on the surface of CdS nanorods. The disappearance of the excitonic feature in CdS NRs at this stage is attributed to the delocalization of carriers into small gold clusters and oleate complexes that form on the semiconductor surface. Spectral changes occurring during the initial heating of the mixture are accompanied by the visible change of the solution color from yellow to light brown, while further heating of the flask to above 100 °C results in additional darkening of the solution and correlated increase in the amplitude of the absorption tail (for $\lambda > 500$ nm). At this stage of the reaction, the average size of the Au tip reaches 4 nm, giving rise to a small absorption feature at $\lambda = 550$ nm, corresponding to the surface plasmon resonance in Au nanoparticles [143–145].

We now consider a more detailed analysis employing femtosecond transient absorption spectroscopy to investigate the dynamics of exciton–plasmon interaction in epitaxial composites of Au and CdS domains exhibiting strong domain

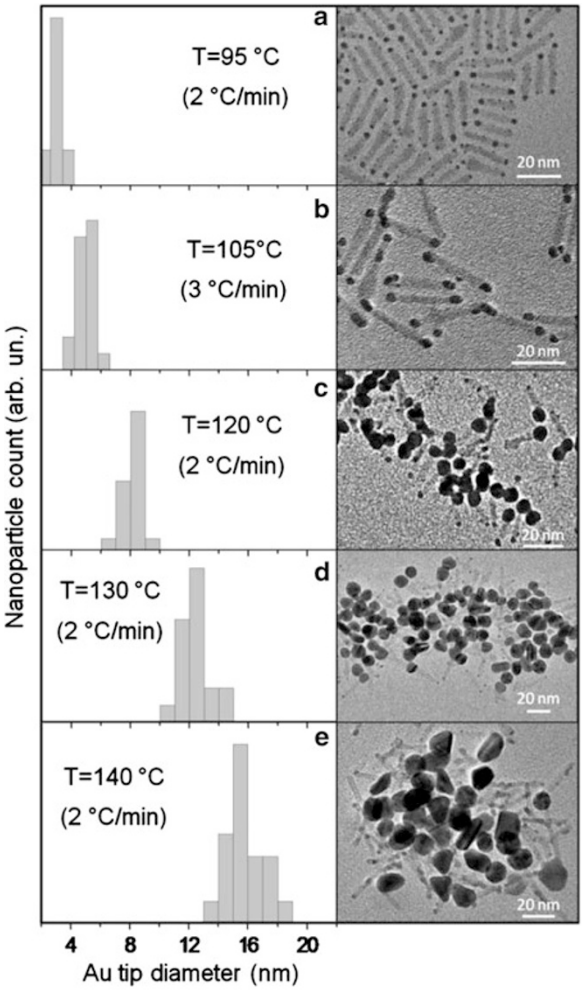

Fig. 13.16 Histogram (*left*) and TEM (*right*) of Au/CdS nanocomposites grown at five different temperatures. Average Au domain sizes are (**a**) d = 3.15 nm, (**b**) d = 4.87, (**c**) d = 8.7 nm, (**d**) d = 12.6 nm, and (**e**) d = 15.67 nm (Reprinted with permission from Khon et al. [106]. Copyright 2010 American Chemical Society)

coupling [138]. First, the steady-state and time-resolved optical properties of isolated Au and CdS nanocrystals are reexamined in Fig. 13.17. The absorbance of CdS nanorods (Fig. 13.17c) shows a characteristic excitonic edge at 465 nm, corresponding to the lowest energy 1S(e)-$1S_{3/2}$(h) transition in these structures.

The chirp-corrected transient absorption spectra (Fig. 13.17d), resulting from the excitation of CdS nanorods with 120-fs laser pulses (λ_{exc} = 340 nm), show an expected dominant bleaching associated with higher probability 1S(e)-$1S_{3/2}$(h) transitions as well as a lower magnitude bleaching corresponding to higher energy excitations between 1P(e)-$1P_{3/2}$(h) states. Spectral distortion due to the Shark effect was not observed in these measurements due to relatively low excitation intensities, corresponding to a linear power dependence regime. A negligible contribution of the Stark effect into the observed bleach dynamics is also consistent with the

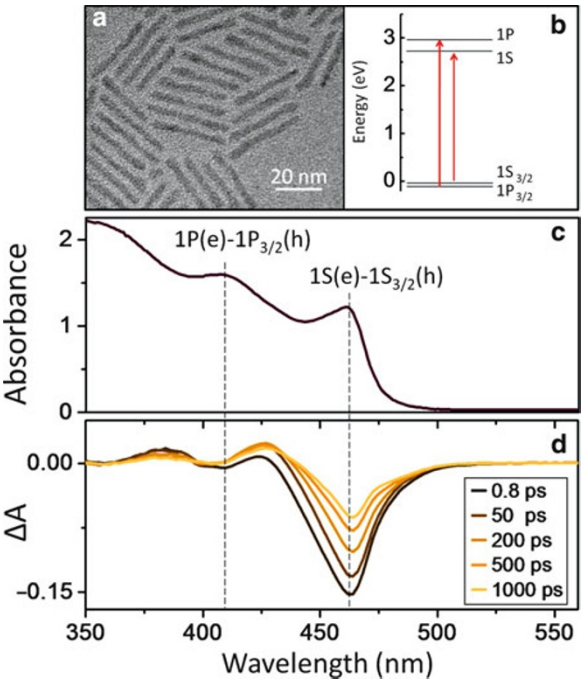

Fig. 13.17 (**a**) TEM image of CdS nanorods used for seeding the growth of Au domains. (**b**) Energy diagram showing the two lowest energy transitions in CdS NRs, corresponding to the excitation of 1S(e)-$1S_{3/2}$(h) and 1P(e)-$1P_{3/2}$(h) excitons, distinguishable in the absorbance spectra of CdS NRs (**c**), as the two broad-range peaks. (**d**). Temporal changes in the absorbance of CdS NRs induced by 340-nm excitation pulses. The negative signal around $\lambda \approx 465$ nm, known as spectral bleach, is produced by the excitation of 1S(e)$1S_{3/2}$(h) transitions, while a smaller negative signal at $\lambda \approx 410$ nm corresponds to the formation of 1P(e)$1P_{3/2}$(h) excitons (Reprinted with permission Khon et al. [138]. Copyright 2011 American Chemical Society)

absence of a positive transient absorption signal at early probe times ($\tau < 1$ ps). The observed changes in the absorption of CdS nanocrystals (ΔA) are chiefly the result of photoinduced electrons, as anticipated due to comparatively low effective masses of these carriers in bulk CdS [146, 147] and high degeneracy of hole states in CdS nanocrystals. The restoration of the 1S(e)-$1S_{3/2}$(h) bleach is achieved via both radiative decay and the trapping of excited carriers on nanorod surfaces, where approximately half of the initial carrier population in the 1S(e) excited state is recovered after 300 ps [148].

The absorption spectra of isolated Au nanoparticles are examined in Fig. 13.18. As a result of the resonant nature of surface plasmons, the frequency is dependent on the composition, size, and shape of metal nanoparticles, as well as their dielectric environment. To gain a better understanding of how the size of Au nanoparticles affects the transient and steady-state absorption of surface plasmons, samples consisting of three different Au nanoparticle diameters are compared. Furthermore, the Au nanoparticle diameters for these measurements are chosen to

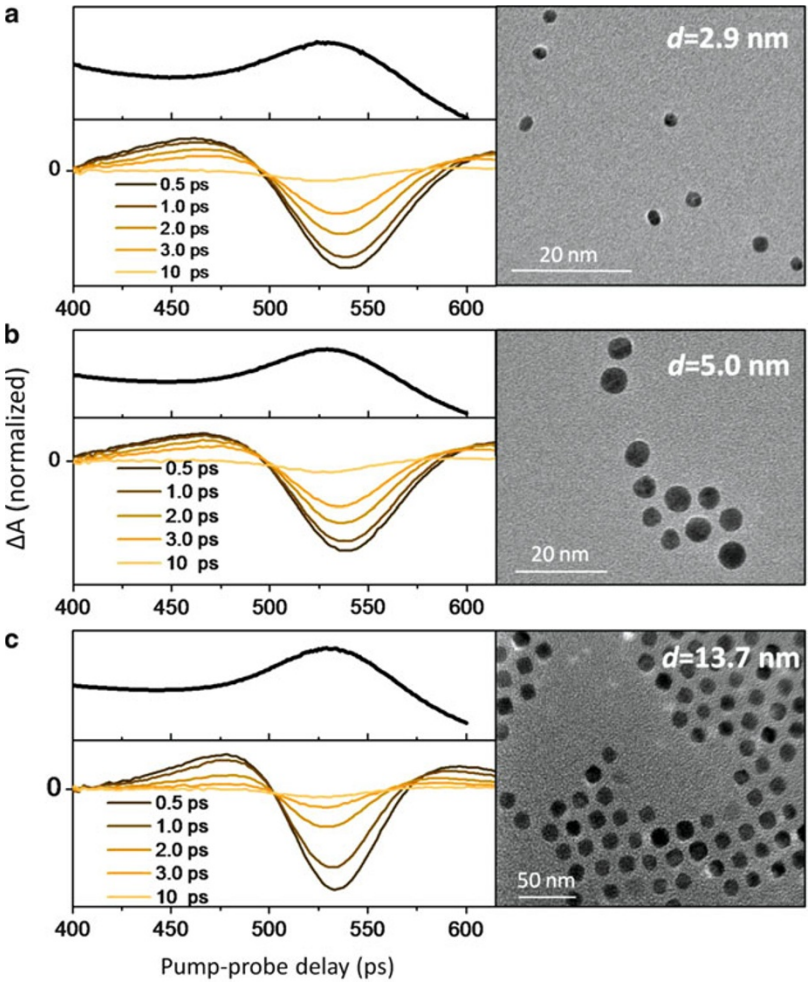

Fig. 13.18 Steady-state and transient absorption spectra of isolated Au domains, corresponding to three different nanoparticle sizes: (**a**) 2.9 nm, (**b**) 5.0 nm, and (**c**) 13.7 nm (Reprinted with permission Khon et al. [138]. Copyright 2011 American Chemical Society)

correspond with the size range of the Au domains in the heteroepitaxial Au/CdS nanocomposites soon to be examined. According to Fig. 13.18, plasmon resonance occurs in each of the three samples of isolated Au nanoparticles, observed as a broad-range absorption peak in the steady-state spectra with corresponding maxima in the vicinity of 530 nm. A moderate variation in the spectral position of the plasmon resonance between the individual measurements is consistent with the size-dependent characteristics of plasma oscillations according to Mie theory [149].

The transient absorption spectra ($\lambda_{exc} = 400$ nm) attributed to isolated Au nanocrystals of respective diameters show a pronounced bleach correlated to the

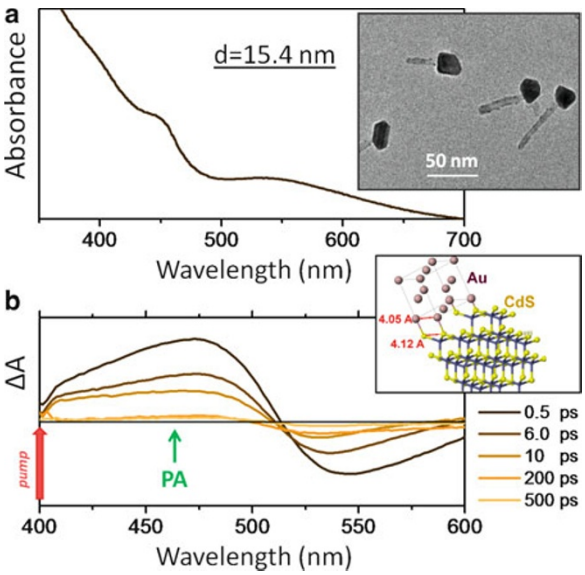

Fig. 13.19 (**a**) Steady-state absorption of Au/CdS heterostructures comprising 15.7-nm Au domains. A representative TEM image is shown in the *insert*. (**b**) Transient absorption spectra of 15.7-nm-Au/CdS nanocomposites resulting from the excitation at $\lambda = 400$ nm with 120 fs pump pulses. The recovery of ΔA shows an expected plasmonic feature, which resembles the corresponding TA dynamics of isolated Au nanoparticles. Surprisingly, bleaching of lowest energy excitons in CdS domains is not observed for any pump-probe delay (Reprinted with permission Khon et al. [138]. Copyright 2011 American Chemical Society)

steady-state absorption maxima. This negative ΔA signal in the transient absorption spectra of isolated Au nanoparticles has been previously ascribed to the excitation-induced broadening of the plasmon peak, which causes the transient absorption spectra to form a characteristic valley at the plasmon wavelength flanked by the two positive low amplitude peaks [150, 151]. Such broadening of the plasmon absorbance results from higher order multipole plasma oscillations (e.g., quadrapole) in Au nanoparticles induced by the excitation pulse. Notably, the central dip in the transient spectra is observed for all investigated gold samples, which further confirms the presence of resonant excited carrier oscillations in these nanoparticles.

To study the optical characteristics of exciton–plasmon interactions in Au/CdS composites, gold domains representing different diameters were grown directly onto colloidal CdS nanorods. To begin the assessment of the charge carrier dynamics, matchstick shaped Au/CdS nanocomposites comprising a large-diameter Au domain ($d = 15.4$ nm) were analyzed first (see Fig. 13.19). In order to achieve an efficient excitation of carriers in both domains of the heterostructure, a 400-nm excitation pulse is utilized, whereby delivering sufficient photon energy for the simultaneous excitation of 1S excitons in CdS ($\lambda = 465$ nm) and plasmons in Au domains ($\lambda = 530$ nm).

The transient absorption spectra of Au/CdS matchsticks in Fig. 13.19b shows spectrally broad bleaching of the absorption profile around $\lambda = 540$ nm, corresponding to plasmon oscillations in Au domains (note that *x*-scales in (a) and (b) are different). The magnitude of this bleach reaches its maximum in less than 500 fs, driven primarily by excitations of hot carriers and simultaneous fast cooling of the nonequilibrium carrier population via electron–electron interaction and subsequently recovers to $\Delta A(\lambda) = 0$ in 500 ps. While the observed plasmon bleaching kinetics are in agreement with the transient absorption spectra of isolated Au nanoparticles, there is now no evidence of bleaching at 465 nm, which would be associated with the formation of excitons in the CdS domain of the heterostructure. In fact, contrary to the transient absorption profile of pure CdS nanorods, which show a well-defined $1S(e)\text{-}1S_{3/2}(h)$ bleach ($\Delta A/A = -0.15$), the amplitude of Au/CdS nanocomposites in the same wavelength range is positive (green arrow in Fig. 13.19b) demonstrating a photodarkening effect, rather than bleaching.

The lack of excitonic features corresponding to $1S(e)\text{-}1S_{3/2}(h)$ transitions in Au/CdS composites can explain the regularly observed quenching of fluorescence emission in semiconductor domains [46, 152–155] However, a generally accepted explanation ascribing the origin of this fluorescence quenching in semiconductor domains to the photoinduced transfer of 1S(e) electrons into Au does not seem compelling considering the full suppression of the CdS bleach. If electron transfer was the dominant process depleting the population of 1S(e) states in CdS, a significant portion of excited electrons would still be present in the 1S(e) state after 500 fs, as the interfacial transfer rate of carriers is generally slow enough to be observed using transient absorption spectroscopy ($\tau(e) > 350$ fs, $\tau(h) > 650$ fs) [148, 156–159] Furthermore, electron transfer processes alone cannot account for the appearance of a positive transient absorption signal spanning such a broad wavelength range (400–520 nm), which is not present in the transient absorption spectra of isolated Au and CdS domains. The decay of the positive spectral feature provides hints as to the nature of the processes underpinning the carrier dynamics in Au/CdS nanocomposites, as the slow recovery (>100 ps) strongly suggests a contribution from the photoinduced absorption of excited carriers either in the Au or CdS domain.

Overall, the observed transient absorption spectra of Au/CdS composites comprising large-diameter gold domain (Fig. 13.19) are fundamentally different from those of its constituent isolated Au and CdS nanoparticles, exemplified both by the replacement of a bleaching signal in the semiconductor component with photoinduced absorption and the relatively weak bleaching of the surface plasmon feature in Au. To acquire a more informed understanding of the origin of this complex carrier dynamic, Au/CdS heterostructures constructed of smaller size Au domains are examined next.

Figure 13.20 shows the steady-state and transient absorption spectra of Au/CdS heterostructures comprising 5.3-nm Au nanoparticles. The steady-state spectra are rather featureless, exhibiting neither a surface plasmon peak nor the characteristic CdS absorbance edge. Furthermore, in the transient absorption spectra, bleaching of the surface plasmon resonance in Au domains is no longer identifiable, which

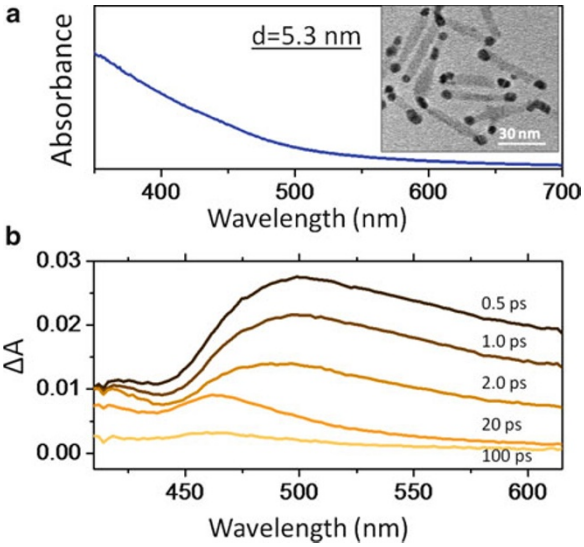

Fig. 13.20 (**a**) Steady-state absorption of Au/CdS heterostructures comprising 5.3-nm Au domains. A representative TEM image is shown in the insert. (**b**) Temporal evolution of the TA spectra for 5.3-nm-Au/CdS nanocomposites excited at $\lambda = 400$ nm. The TA trend contrasts the recovery dynamics observed in isolated Au and CdS nanoparticles, for which both excitonic and plasmonic features are manifested by the prominent dip in ΔA. Instead, the value of ΔA observed for Au/CdS nanocomposites remains positive throughout the entire spectral range of the probe beam (Reprinted with permission Khon et al. [138]. Copyright 2011 American Chemical Society)

strongly contrasts the dynamics of isolated nanoparticles (see Fig. 13.18) exhibiting an apparent plasmon bleach at $\lambda = 530$ nm. These dramatic alterations to the spectral profiles indicate that the nature of excited electron oscillations in smaller Au domains is now modified due to direct coupling of CdS nanocrystals.

In addition to the termination of the surface plasmon feature, the transient absorption spectra reveals a broad positive signal, which, in comparison with the transient absorption characteristics of 15.4-nm Au/CdS heterostructures, extends across the entire spectral range of the probe pulse. The recovery of this feature is too slow to be interpreted as a nonlinear modification of the spectral profile due to local fields and thus, similar to the case of 15.4-nm Au/CdS heterostructures, is attributed to the photoinduced absorption of excited carriers occupying electronic states within the CdS band gap. Note that decreasing the size of gold domains from 15.4 to 5.3 nm results in the onset of a semiconductor excitonic feature, appearing as a characteristic dip at $\lambda < 450$ nm, corresponding to the excitation of ground-state excitons, $1S(e)\text{-}1S_{3/2}(h)$, but this excitonic bleach is substantially weaker than that of pure CdS nanorods and is offset by the positive background of the broad photoinduced absorption.

Lastly, nanostructures in which the size of Au domains is only 2.7 nm (see Fig. 13.21) are considered. This specific architecture acts as a transitional system that spans the link between optical properties of pure CdS nanorods and those of

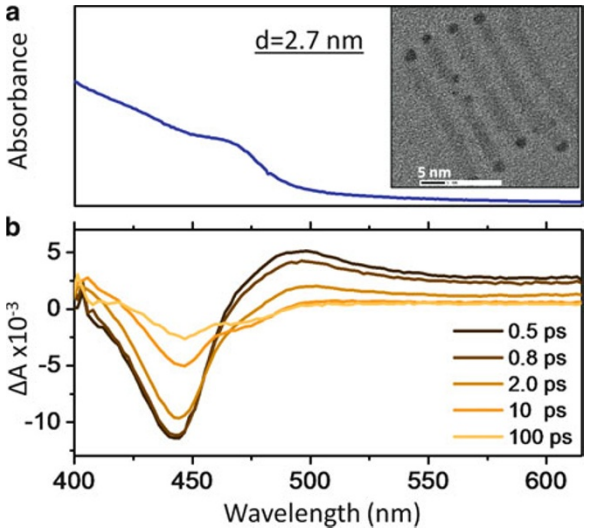

Fig. 13.21 (**a**) Steady-state absorption of Au/CdS heterostructures comprising 2.7-nm Au domains (a typical TEM image is shown in the *insert*). (**b**) Temporal evolution of the TA spectra for 2.7-nm Au/CdS nanocomposites resulting from the excitation at $\lambda = 400$ nm with 120 fs pump pulses. The negative ΔA signal at $\lambda \approx 445$ nm corresponds to bleaching of band gap transitions in CdS. Its spectral position is blue-shifted from the corresponding excitonic edge in the steady-state spectrum, which is believed to be caused by the positive contribution of the photoinduced absorbance into ΔA at the low-energy side of the excitonic peak. The absence of the plasmon bleach at $\lambda = 560$ nm is interpreted as a suppression of plasmon oscillations (Reprinted with permission Khon et al. [138]. Copyright 2011 American Chemical Society)

5.3-nm Au/CdS nanocomposites and exhibits several unique properties, including suppression of the plasmon bleach, suppression of excitonic features in CdS, and spectrally broad photoinduced absorption.

Similar to 5.3-nm Au/CdS heterostructures, transient absorption spectra of Au/CdS nanocomposites comprising 2.7-nm Au tips (Fig. 13.21b) do not indicate any spectral bleaching in the $\lambda = 530$ nm range. Also, just as in the case of nanocomposites with larger tip sizes, the suppression of plasmons in 2.7-nm Au/CdS heterostructures contrasts the carrier dynamics for the control sample of isolated 2.7-nm Au nanoparticles (Fig. 13.18), for which the presence of the plasmon resonance is observed in both steady-state and time-resolved absorption measurements.

To explain the observed suppression of plasmons in Au domains, we consider a "low-barrier" coupling between Au and CdS components, for which Au electrons with energies located above the Fermi level (plasmon band) are not sufficiently confined by the Au/CdS interface to exhibit resonant oscillations. The validity of this assumption is supported by the fact that the interface of the two nanosized domains consists of just a few monolayers and thus cannot form a substantial potential barrier and the fact that energies of conduction electrons in Au domains are raised relative to their respective positions in isolated Au nanoparticles due to

charging. Indeed, the photoinduced transfer of excited electrons from CdS to Au leaves Au domains with an excess negative charge, which equalizes the energy difference between the conduction states in both domains. As a result, electronic wavefunctions of conduction carriers in S and charged M domains partly overlap, giving rise to mixing of electronic states at the interface and corresponding changes in the density of states in both materials. For small-diameter Au nanoparticles, such mixing results in the delocalization of the plasma electrons into CdS portion of nanocomposites, which has a substantially greater volume, and therefore can significantly reduce the boundary effect in Au nanoparticles. Such delocalization-induced suppression of the plasmon resonance in Au NPs is further supported by steady-state absorption spectra of 2.7- and 5.3-nm Au/CdS nanocomposites through the absence of distinct plasmon features. These time-independent measurements rule out nonlinear excitation effects as a potential origin of plasmon suppression since excitation intensities used in steady-state absorption experiments are orders of magnitude below those used in ultrafast studies.

The proposed mixing of the electronic states at the interface of Au and CdS domains can also explain the existence of a positive transient absorption signal observed for all investigated Au/CdS samples. Indeed, due to strong coupling of semiconductor and metal domains, carrier excitations in CdS can lead to the population of CdS-modified conduction states of Au, which will then serve the role of interfacial trap states. This process can occur on a timescale faster than the pulse duration, as can be expected from the general nature of excitation processes in nanocrystals, and will therefore contribute into the "instantaneous" photoinduced absorption of Au/CdS nanocomposites, manifested by the positive ΔA.

While the suppression of plasmons in Au domains can be explained in terms of delocalization of conduction states across the Au/CdS interface, the absence of the excitonic features in the transient absorption and steady-state spectra can, likewise, be attributed to tunneling of CdS carriers into Au domains. Indeed, for small-diameter Au tips, the delocalization of CdS electrons into metal is limited to a few nanometers, which is insufficient to alter the character of quantum confinement in CdS, as can be confirmed by nearly unsuppressed CdS bleach in 2.7-nm Au/CdS spectra (Fig. 13.21b); meanwhile, large-size Au domains allow for a substantial delocalization of 1S(e) CdS wavefunctions into metal, thus leading to the suppression of excitonic features. Expectedly, the correlation between the degree of exciton suppression and the size of Au domains is opposite to that of plasmon suppression, which is the strongest when the size of Au tips is the smallest.

5.2.2 ZnSe- and ZnTe-Seeded CdS Nanorods Supporting Platinum Tips

The ZnTe/CdSe/CdS/Pt and ZnSe/CdS/CdS/Pt core/shell/rod/tip nanocomposites are one of the more complex nanocomposite structures, combining several type II semiconductor–semiconductor junctions with a metal–semiconductor interface [74]. These structures are capable of driving photocatalytic reactions for production of solar hydrogen. Excitons created by absorbed photons are quickly separated by the energy gradient of the type II semiconductor nanorod, where the electron is then injected into the Pt tip, which has a sufficient energy to reduce H_2O, producing H_2 gas.

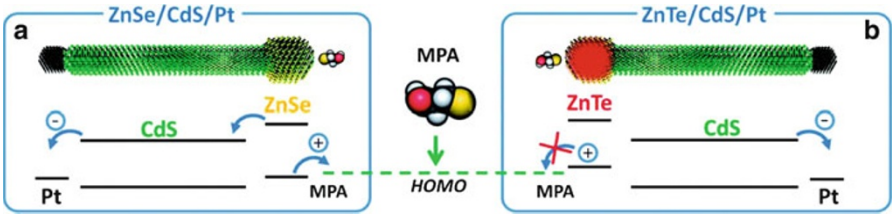

Fig. 13.22 Electronic level diagram showing a relative alignment of excited state energies in ZnSe/CdS/Pt (**a**) and ZnTe/CdS/Pt (**b**) heteronanocrystals. Upon excitation, an electron–hole pair is efficiently separated at hetero-interfaces of the two semiconductor materials with electrons residing in the CdS and holes in the ZnSe(Te) domain of the structure. Subsequently, photoinduced holes undergo further localization, character of which is determined by the relative alignment of hole energies at the semiconductor–ligand interface. For instance, in the case of ZnSe-terminated nanorods, the photoinduced hole is accepted by the ligand molecule mercaptopropionic acid (*MPA*) and expelled to the surface of the composite nanoparticle, while for ZnTe-terminated nanorods, the hole is confined inside the semiconductor domain (Reprinted with permission Acharya et al. [74]. Copyright 2011 American Chemical Society)

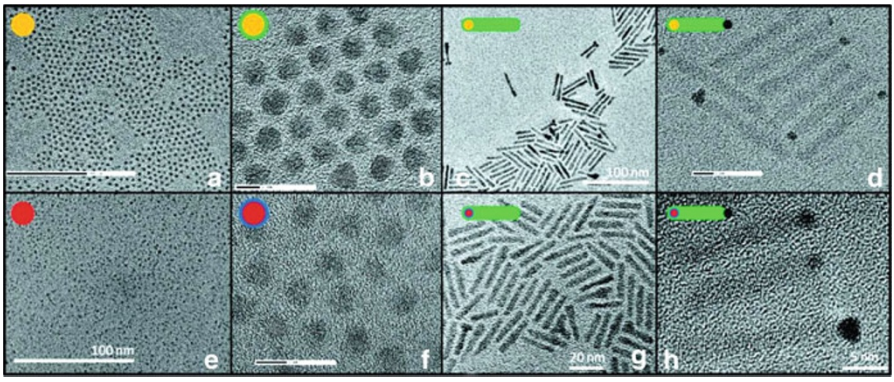

Fig. 13.23 Transmission electron microscope (*TEM*) images of ZnSe/CdS/Pt and ZnTe/CdS/Pt heteronanocrystals corresponding to the four consecutive stages of the growth protocol. (**a**) ZnSe seed NCs. (**b**) ZnSe NCs with a few monolayers of the CdS shell. (**c**) ZnSe/CdS nanorods grown from ZnSe/CdS core/shell NCs. (**d**) ZnSe/CdS nanorods after Pt deposition. (**e**) ZnTe NCs. (**f**). ZnTe/CdSe core/shell NCs. (**g**) ZnTe/CdSe/CdS nanorods grown from ZnTe/CdSe seeds. (**h**) ZnTe/(CdSe)/CdS nanorods after Pt deposition (Reprinted with permission Acharya et al. [74]. Copyright 2011 American Chemical Society)

While electrons undergo similar transitions in both ZnTe/CdSe/CdS/Pt and ZnSe/CdS/CdS/Pt systems through the charge transfer into a Pt tip, the photoinduced hole in ZnTe-seeded nanorods is bound to the core structure, while in ZnSe-seeded nanorods, it localizes on the surface (Fig. 13.22). This serves to protect the latter structure from photooxidation effects that would otherwise destroy the sulfide semiconductor, as is the fate of the ZnTe/CdSe nanorods.

The syntheses of both structures are similar to the previously covered protocols for ZnSe/CdS heteronanorods, which begins with the nucleation of the cores, followed

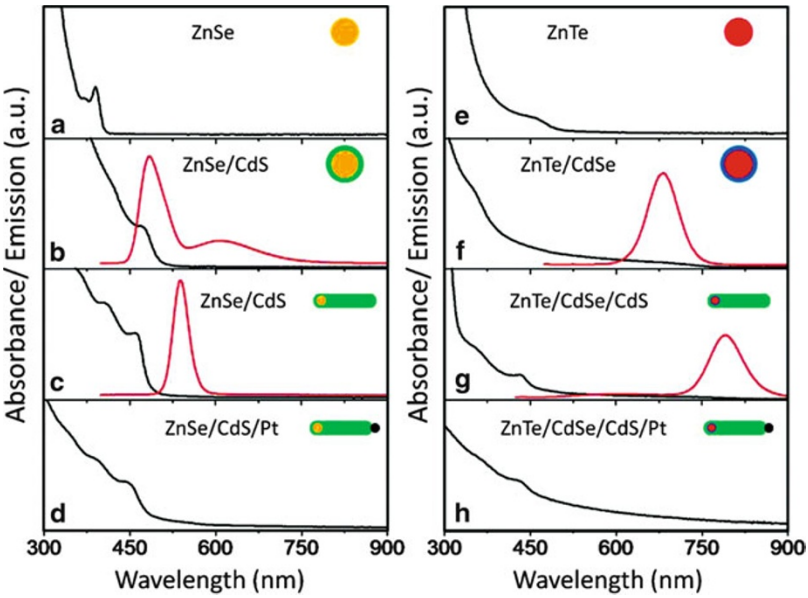

Fig. 13.24 Optical properties of fabricated heteronanocrystals. (**a**) The absorbance of ZnSe NCs showing an excitonic feature at $\lambda = 390$ nm. Band-edge emission was not observed for these samples. (**b**) ZnSe NCs overcoated with a 1-nm-thick shell of CdS, for which the onset of quasi-type II carrier confinement regime is evidenced through red-shifted absorption ($\lambda \approx 475$ nm) and emission peaks ($\lambda \approx 490$ nm). (**c**) Emission and absorbance of ZnSe/CdS nanorods grown from ZnSe/CdS core/shell NCs. (**d**) Absorbance of ZnSe/CdS nanorods after Pt deposition. (**e**)–(**h**) Emission and absorbance spectra associated with the four-step synthesis of ZnTe/CdS/CdS/Pt heteronanocrystals: (**e**) ZnTe NCs, (**f**) ZnTe/CdSe core/shell NCs, (**g**) ZnTe/CdSe/CdS nanorods grown from ZnTe/CdSe seeds, and (h) ZnTe/(CdSe)/CdS nanorods after Pt deposition (Reprinted with permission Acharya et al. [74]. Copyright 2011 American Chemical Society)

by the epitaxial growth of the shells, and continues with the anisotropic growth of an "arm." The reaction is now taken a step further to include the growth of small Pt tips onto one end of heteronanorods by reacting a Pt salt [74] (Fig. 13.23).

According to Fig. 13.24, ZnTe core nanocrystals initially exhibit an absorbance feature near 450 nm. The growth of the CdSe shell results in red-shifting of this absorbance feature and the onset of the type II emission around 700 nm (Fig. 13.24f).

The growth of the nanorod "arm" adds the familiar CdS absorbance edge at 450 nm, with the type II emission red-shifting further to about 800 nm (Fig. 13.24g). For clarification, as always, each step of the synthesis that increases the size in any or all directions that exhibit quantum confinement will result in a relatively small but detectable red shift of optical properties.

As ZnSe/CdS heteronanorods have already been analyzed in a previous section, only a brief summary will be provided here. For the detailed analysis of ZnSe/CdS structures, see section "CdSe Seeded CdS Nanorods and Nanotetrapods: Quasi-Type II Heterostructure." Growth of the CdS quenches the violet fluorescence of

the binary ZnSe core and introduces type II fluorescence of the ZnSe/CdS. As the CdS portions are synthesized, trap state emission is suppressed. Note that by this stage of the synthesis, the final absorption spectrum is similar to the superposition of each individual component of the spectra.

The most noticeable change in the optical characteristics resulting from deposition of Pt tips is the complete quenching of the fluorescence in both heteronanorod structures. This is caused by a combination of effects from photoinduced charge transfer of electrons into the metals Pt domain and the trapping of charge carriers at the CdS/Pt junction. The absorption spectra of both nanocomposites are also altered, marked by an apparent widening of the CdS excitonic feature spectra and an increase in low-energy emission observed as a long, featureless tail extending out into the infrared.

With this, we conclude the analysis of metal–semiconductor nanocomposites.

6 Future Perspectives

Design and synthesis of nanocomposite structures for enhancing optical properties of colloidal nanomaterials is a fast developing area of material science, which progress is fueled both by the fundamental significance of underlying intra-domain processes and the technological applicability of multicomponent nanostructures in the next generation optoelectronics.

The use of composite nanocrystals as fluorescent tags in biological and biomedical applications will continue to evolve. The two major avenues for the future expansion are viewed to be the employment of nontoxic semiconductors for core/shell nanocrystal bio-labels to aid either in vivo imaging applications or the development of composite nanocrystal probes for the transduction of electric potential changes in membranes of living cells (so-called action potential). The latter may lead to the construction of neural activity maps, which is of critical importance to the treatment of such neurological disorders as Alzheimer's or Parkinson's diseases.

Another possible avenue for the future development of nanocomposite's optical properties concerns the investigation and possible practical applications of the exciton–plasmon interactions in metal–semiconductor heterostructures. Indeed, such interaction allows for an enhanced harvesting of light through the plasmon-assisted mechanism, which energy is then transferred to the semiconductor counterpart. This may improve the efficiency of nanocrystal emitters in such devices as LEDS or lasers. On the other hand, plasmon's role of a light-harvesting antenna should enable an increased absorbance of light in photovoltaic and photocatalytic devices. At present, the exciton–plasmon interaction is well understood in a weak coupling regime, while strongly coupled exciton–plasmon interactions still present significant challenges both for the theoreticians in the attempt to describe the resulting system behavior and for experimentalists in their effort to fabricate functional metal–semiconductor tandems with strong exciton–plasmon coupling.

In addition to the aforementioned prospects for nanocomposite development, there are several other emerging directions that take an advantage of optical properties of multi-domain nanocrystals. The use of heterostructured nanorods appended with Pt tips, for instance, has been demonstrated to produce hydrogen from water under visible light. These structures may thus be developed as alternative catalysts for either H_2 production or CO_2 reduction under visible light. The use of composite nanocrystals has also been considered for such application as electroabsorption modulators, optical switches, and photodetectors. As always, the primary challenges on the way toward the realization of these prospects are synthetic in nature. The evolving ability to control the inter-domain stoichiometry and development of unified, scalable, and reproducible synthetic protocols is of paramount importance in establishing the control over optical properties of nanocomposites. Solving these challenges will undoubtedly contribute both to the technological applications of these multifunctional materials and to the fundamental understanding of electronic processes at composite nano-interfaces.

References

1. Klimov VI, Ivanov SA, Nanda J, Achermann M, Bezel I, McGuire JA, Piryatinski A (2007) Single-exciton optical gain in semiconductor nanocrystals. Nature 447:441
2. Hillhouse HW, Beard MC (2009) Solar cells from colloidal nanocrystals: fundamentals, materials, devices, and economics. Curr Opin Coll Int Sci 14:245
3. Gur I, Fromer NA, Geier ML, Alivisatos AP (2005) Air-stable all-inorganic nanocrystal solar cells processed from solution. Science 310:462
4. Borensztein Y, Delannoy L, Djedidi A, Barrera RG, Louis C (2010) Monitoring of the plasmon resonance of gold nanoparticles in Au/TiO_2 catalyst under oxidative and reducing atmospheres. J Phys Chem C 114:9008–9021
5. Amirav L, Alivisatos AP (2010) Photocatalytic hydrogen production with tunable nanorod heterostructures. J Phys Chem Lett 1:1051–1054
6. Coe S, Woo WK, Bawendi M, Bulovic V (2002) Electroluminescence from single monolayers of nanocrystals in molecular organic devices. Nature 420:800
7. Tessler N, Medvedev V, Kazes M, Kan SH, Banin U (2002) Efficient near-infrared polymer nanocrystal light-emitting diodes. Science 295:1506
8. Steckel JS, Snee P, Coe-Sullivan S, Zimmer JR, Halpert JE, Anikeeva P, Kim LA, Bulovic V, Bawendi MG (2006) Color-saturated green-emitting QD-LEDs. Angew Chem Int Ed 45:5796
9. Colvin VL, Schlamp MC, Alivisatos AP (1994) Light-emitting diodes made from cadmium selenide nanocrystals and a semiconducting polymer. Nature 370:354
10. Schlamp MC, Peng XG, Alivisatos APJ (1997) Improved efficiencies in light emitting diodes made with CdSe(CdS) core/shell type nanocrystals and a semiconducting polymer. Appl Phys 82:5837
11. Mattoussi H, Radzilowski LH, Dabbousi BO, Thomas EL, Bawendi MG, Rubner MF (1998) Properties of CdSe nanocrystal dispersions in the dilute regime: structure and interparticle interactions. J Appl Phys 83:7965
12. Medintz IL, Uyeda HT, Goldman ER, Mattoussi H (2005) Quantum dot bioconjugates for imaging, labelling and sensing. Nature Mat 4:435
13. Mattoussi H, Mauro JM, Goldman ER, Anderson GP, Sundar VC, Mikulec FV, Bawendi MG (2000) Self-assembly of CdSe – ZnS quantum dot bioconjugates using an engineered recombinant protein. J Am Chem Soc 122:12142

14. Bruchez JM, Moronne M, Gin P, Weiss S, Alivisatos AP (1998) Semiconductor nanocrystals as fluorescent biological labels. Science 281:2013
15. Wang RY, Feser JP, Lee JS, Talapin DV, Segalman R, Majumdar A (2008) Enhanced thermopower in PbSe nanocrystal quantum dot superlattices. Nano Lett 8:2283
16. Kovalenko MV, Scheele M, Talapin DV (2009) Colloidal nanocrystals with molecular metal chalcogenide surface ligands. Science 324:1417
17. Ridley BA, Nivi B, Jacobson JM (1999) All-inorganic field effect transistors fabricated by printing. Science 286:746
18. Lee S, Jeong S, Kim D, Park BK, Moon J (2007) Superlattices. Microstruct 42:361
19. Schneider JJ, Hoffmann RC, Engstler J, Soffke O, Jaegermann W, Issanin A, Klyszcz A (2008) A printed and flexible field-effect transistor device with nanoscale zinc oxide as active semiconductor material. Adv Mater 20:3383
20. Talapin DV, Mekis L, Gotzinger S, Kornowski A, Benson O, Weller H (2004) CdSe/CdS/ZnS and CdSe/ZnSe/Zns core-shell-shell nanocrystals. J Phys Chem B 108:18826
21. Talapin DV, Murray CB (2005) PbSe nanocrystal solids for n- and p-channel thin film field-effect transistors. Science 310:86
22. Lee JS, Shevchenko EV, Talapin DV (2008) Au-PbS core-shell nanocrystals: plasmonic absorption enhancement and electrical doping via interparticle charge transfer. J Am Chem Soc 130:9673
23. Erwin SC, Zu LJ, Haftel MI, Efros AL, Kennedy TA, Norris DJ (2005) Doping semiconductor nanocrystals. Nature 436:91
24. Salgueirino-Maceira V, Correa-Duarte MA (2007) Increasing the complexity of magnetic core/shell structured nanocomposites for biological applications. Adv Mater 19:4131
25. Son DI, Kim JH, Park DH, Choi WK, Li F, Ham JH, Kim TW (2008) Nonvolatile flexible organic bistable devices fabricated utilizing CdSe/ZnS nanoparticles embedded in a conducting poly N-vinylcarbazole. Nanotechnology 19:055204
26. Liz-Marzan LM, Mulvaney P (2003) The assembly of coated nanocrystals. J Phys Chem B 107:7312
27. Das BC, Batabyal SK, Pal AJ (2007) A bit per particle: electrostatic assembly of CdSe quantum dots as memory elements. Adv Mater 19:4172
28. Das BC, Pal AJ (2008) Memory applications and electrical bistability of semiconducting nanoparticles: do the phenomena depend on bandgap? Small 4:542
29. Ghosh B, Sahu S, Pal AJ (2008) Core-shell nanoparticles: an approach to enhance electrical bistability. J Phys Chem C 112:11290
30. Reiss P, Protiere M, Li L (2009) Core/shell semiconductor nanocrystats. Small 5:154
31. Cozzoli PD, Pellegrino T, Manna L (2006) Synthesis, properties and perspectives of hybrid nanocrystal structures. Chem Soc Rev 35:1195
32. Yao WT, Yu SH (2008) Synthesis of semiconducting functional materials in solution: from II-VI semiconductor to inorganic–organic hybrid semiconductor nanomaterials. Adv Funct Mater 18:3357
33. Talapin DV, Lee J-S, Kovalenko MV, Shevchenko EV (2010) Prospects of nanocrystal solids as electronic and optoelectronic materials. Chem Rev 110:389–458
34. Kumar S, Jones M, Lo SS, Scholes GD (2007) Nanorod heterostructures showing photoinduced charge separation. Small 3:1633
35. Carbone L, Nobile C, Giorgi MD, Sala FD, Morello G, Pompa P, Hytch M, Snoeck E, Fiore A, Franchini IR, Nadasan M, Silvestre AF, Chiodo L, Kudera S, Cingolani R, Krahne R, Manna L (2007) Synthesis and micrometer-scale assembly of colloidal CdSe/CdS nanorods prepared by a seeded growth approach. Nano Lett 7:2942
36. Dorfs D, Salant A, Popov I, Banin U (2008) ZnSe quantum dots within CdS nanorods: a seeded-growth type-II system. Small 4:1319
37. Lo SS, Khan Y, Jones M, Scholes GD (2009) Temperature and solvent dependence of CdTe/CdSe heterostructure nanorod spectra. J Chem Phys 131:084714

38. Zhong H, Scholes GD (2009) Shape tuning of type II CdTe-CdSe colloidal nanocrystal heterostructures through seeded growth. J Am Chem Soc 131:9170–9191
39. Shieh F, Saunders AE, Korgel BA (2005) General shape control of colloidal CdS, CdSe, CdTe quantum rods and quantum rod heterostructures. J Phys Chem B 119:8539
40. Halpert JE, Porter VJ, Zimmer JP, Bawendi MG (2006) Synthesis of CdSe/CdTe nanobarbells. J Am Chem Soc 128:12590
41. Kirsanova M, Nemchinov A, Hewa-Kasakarage NN, Schmall N, Zamkov M (2009) Synthesis of ZnSe/CdS/ZnSe nano-barbells showing photoinduced charge separation. Chem Mater 21:4305
42. Shi W, Zeng H, Sahoo Y, Ohulchanskyy TY, Ding Y, Wang ZL, Prasad PN (2006) A general approach to binary and ternary hybrid nanocrystals. Nano Lett 6:875
43. Heng Y, Chen M, Rice PM, Wang SX, White RL, Sun S (2005) Dumbbell-like bifunctional Au-Fe_3O_4 nanoparticles. Nano Lett 5:379
44. Carbone L, Kudera S, Carlino E, Parak WJ, Giannini C, Cingolani R, Manna L (2006) Multiple Wurtzite twinning in CdTe nanocrystals induced by methylphosphonic acid. J Am Chem Soc 128:748
45. Milliron DJ, Hughes SM, Cui Y, Manna L, Li JB, Wang LW, Alivisatos AP (2004) Colloidal nanocrystal heterostructures with linear and branched topology. Nature 430:190
46. Mokari T, Rothenberg E, Popov I, Costi R, Banin U (2004) Selective growth of metal tips onto semiconductor quantum rods and tetrapods. Science 304:1787
47. Mokari T, Sztrum CG, Salant A, Rabani E, Banin U (2005) Formation of asymmetric one-sided metal-tipped semiconductor nanocrystal dots and rods. Nature Mater 4:855
48. Carbone L, Kudera S, Giannini C, Ciccarella G, Cingolani R, Cozzoli PD, Manna L (2006) Selective reactions on the tips of colloidal semiconductor nanorods. J Mate Chem 16:3952
49. Menagen G, Macdonald JE, Shemesh Y, Popov I, Banin U (2009) Au growth on semiconductor NAnorods: photoinduced versus thermal growth mechanisms. J Am Chem Soc 131:17406–17411
50. Habas SE, Yang P, Mokari T (2008) Selective growth of metal and binary metal tips on CdS nanorods. J Am Chem Soc 130:3294
51. Peng XG, Schlamp MC, Kadavanich AV, Alivisatos AP (1997) Epitaxial growth of highly luminescent CdSe/CdS core/shell nanocrystals with photostability and electronic accessibility. J Am Chem Soc 119:7019
52. Hines MA, Guyot-Sionnest P (1996) Synthesis and characterization of strongly luminescing ZnS-capped CdSe nanocrystals. J Phys Chem 100:468
53. Dabbousi BO, RodriguezViejo J, Mikulec FV, Heine JR, Mattoussi H, Ober R, Jensen KF, Bawendi MG (1997) (CdSe)ZnS core-shell quantum dots: synthesis and optical and structural characterization of a size series of highly luminescent materials. J Phys Chem B 101:9463
54. Zhao JL, Zhang JY, Jiang CY, Bohnenberger J, Basche T, Mews A (2004) Electroluminescence from isolated CdSe/ZnS quantum dots in multilayered light-emitting diodes. J Appl Phys 96:3206
55. Nizamoglu S, Ozel T, Sari E, Demir HV (2007) White light generation tuned by dual hybridization of nanocrystals and conjugated polymers. Nanotechnology 18:065709
56. Bruchez M, Moronne M, Gin P, Weiss S, Alivisatos AP (2013) Semiconductor nanocrystals as fluorescent biological labels. Science 1998:281
57. Son DH, Hughes SM, Yin YD, Alivisatos AP (2004) Cation exchange reactions-in ionic nanocrystals. Science 306:1009
58. Costa-Fernandez JM, Pereiro R, Sanz-Medel A (2006) The use of luminescent quantum dots for optical sensing. Trends Anal Chem 25:207
59. Nirmal M, Dabbousi BO, Bawendi MG, Macklin JJ, Trautman JK, Harris TD, Brus LE (1996) Fluorescence intermittency in single cadmium selenide nanocrystals. Nature 383:802
60. Hohng S, Ha T (2004) Near-complete suppression of quantum dot blinking in ambient conditions. J Am Chem Soc 126:1324

61. Banin U, Bruchez M, Alivisatos AP, Ha T, Weiss S (1999) Evidence for a thermal contribution to emission intermittency in single CdSe/CdS core/shell nanocrystals; Chemla, D. S. J Chem Phys 110:1195
62. Li YC, Zhong HZ, Li R, Zhou Y, Yang CH, Li YF (2006) High-yield fabrication and electrochemical characterization of tetrapodal CdSe, CdTe, and $CdSe_xTe_{1-x}$ nanocrystals. Adv Funct Mater 16:1705
63. Zhou Y, Li YC, Zhong HZ, Hou JH, Ding YQ, Yang CH, Li YF (2006) Hybrid nanocrystal/polymer solar cells based on tetrapod-shaped $CdSe_xTe_{1-x}$ nanocrystals. Nanotechnology 17:4041
64. Zhang Y, Wang LW, Mascarenhas A (2007) "Quantum coaxial cables" for solar energy harvesting. Nano Lett 7:1264
65. Luque A, Marti A, Nozik AJ (2007) Solar cells based on quantum dots: multiple exciton generation and intermediate bands. Mrs Bull 32:236
66. Nemchinov A, Kirsanova M, Hewa-Kasakarage NN, Zamkov M (2008) Synthesis and characterization of type II ZnSe/CdS core/shell nanocrystals. J Phys Chem C 112:9301
67. Doose S (1856) Optical Amplification from Single Excitons in Colloidal Quantum Dots. Small 2007:11
68. Chan Y, Steckel JS, Snee PT, Caruge JM, Hodgkiss JM, Nocera DG, Bawendi MG (2005) Blue semiconductor nanocrystal laser. Appl Phys Lett 86:073102
69. Talapin DV, Mekis I, Götzinger S, Kornowski A, Benson O, Weller H (2004) CdSe/CdS/ZnS and CdSe/ZnSe/ZnS core-shell-shell nanocrystals. J Phys Chem B 108:18826–18831
70. Chen Y, Vela J, Htoon H, Casson JL, Werder DJ, Bussian DA, Klimov VI, Hollingsworth JA (2008) "Giant" multishell CdSe nanocrystal quantum dots with suppressed blinking. J Am Chem Soc 130:5026
71. Pathan HM, Lokhande CD (2004) Deposition of metal chalcogenide thin films by successive ionic layer absorption and reaction (SILAR) method. Bull Mater Sci 27:85
72. Pietryga JM, Werder DJ, Williams DJ, Casson JL, Schaller RD, Klimov VI, Hollingsworth JA (2008) Utilizing the lability of lead selenide to produce heterostructured nanocrystals with bright, stable infrared emission. J Am Chem Soc 130:4879–4885
73. Neo MS, Venkatram N, Li GS, Chin WS, Ji W (2010) Synthesis of PbS/CdS core-shell QDs and their nonlinear optical properties. J Phys Chem C 114:18037–18044
74. Acharya KP, Khnayzer RS, O'Connor T, Diederich G, Kirsanova M, Klinkova A, Roth D, Kinder E, Imboden M, Zamkov M (2011) The role of hole localization in sacrificial hydrogen production by semiconductor-metal heterostructured nanocrystals. Nano Lett 11:2919
75. Hewa-Kasakarage NN, Kirsanova M, Nemchinov A, Schmall N, El-Khoury PZ, Tarnovsky AN, Zamkov M (2009) Radiative recombination of spatially extended excitons in (ZnSe/CdS)/CdS heterostructured nanorods. J Am Chem Soc 131:1328
76. Fisher BR, Eisler HJ, Stott NE, Bawendi MG (2004) Emission intensity dependence and single-exponential behavior in single colloidal quantum dot fluorescence lifetime. J Phys Chem B 108:143
77. Hewa-Kasakarage NN, El-Khoury PZ, Tarnovsky AN, Kirsanova M, Nemitz I, Nemchinov A, Zamkov M (1837) Ultrafast carrier dynamics in Type II ZnSe/CdS/ZnSe nanobarbells. ACS Nano 2010:4
78. Grätzel M (2001) Photoelectrochemical cells. Nature 414:338–344
79. Miller DAB, Chemla DS, Damen TC, Gossard AC, Wiegmann W, Wood TH, Burrus CA (1984) Band-edge electroabsorption in quantum well structures – the quantum-confined Stark effect. Phys Rev Lett 53:2173–2176
80. Kuo1 Y, Lee1 YK, Ge Y, Ren S, Roth JE, Kamins TI, Miller DA, Harris JS (2005) Strong quantum-confined Stark effect in germanium quantum-well structures on silicon. Nature 437:334
81. Reiss P (2007) ZnSe based colloidal nanocrystals: synthesis, shape control, core/shell, alloy and doped systems. New J Chem 31:1843–1852

82. Hunsche S, Dekorsy T, Klimov V, Kurz H (1996) Ultrafast dynamics of carrier-induced absorption changes in highly-excited CdSe nanocrystals. Appl Phys B 62:3–10
83. Ekimov AI, Hache F, Schanne-Klein MC, Ricard D, Flytzanis C, Kudryavtsev IA, Yaveza TV, Rodina AV, Efros AL (1993) Absorption and intensity-dependent photoluminescence measurements on CdSe quantum dots: assignment of the first electronic transitions. J Opt Soc Am B 10:100–106
84. Nirmal M, Norris DJ, Kuno M, Bawendi MG, Efros AL, Rosen M (1995) Observation of the dark excitons in CdSe quantum dots. Phys Rev Lett 75:3728–3731
85. Klimov V, Hunsche S, Kurz H (1994) Biexciton effects in femtosecond nonlinear transmission of semiconductor quantum dots. Phys Rev B 50:8110–8113
86. Klimov VI (2000) Optical nonlinearities and ultrafast carrier dynamics in semiconductor nanocrystals. J Phys Chem B 104:6112–6123
87. Norris D, Sacra A, Murray C, Bawendi M (1994) Measurement of the size dependent hole spectrum in CdSe quantum dots. Phys ReV Lett 72:2612–2615
88. Many A, Goldstein Y, Grover NB (1965) Semiconductor surfaces. North Holland, Amsterdam
89. Nolte DD (1999) Semi-insulating semiconductor heterostructures: optoelectronic properties and applications. J Appl Phys 85:6259–6289
90. Ozgur U, Alivov YI, Liu C, Teke A, Reshchikov MA, Dogan S, Avrutin V, Cho SJ, Morkoc H (2005) A comprehensive review of ZnO materials and devices. J Appl Phys 98:041301
91. Storm HF (1969) Solid-state power electronics in the USA. IEEE Trans Electron Dev ED 16:957
92. Jun Y, Choi J, Cheon J (2006) Shape control of semiconductor and metal oxide nanocrystals through nonhydrolytic colloidal routes. Angew Chem Int Ed 45:3414–3439
93. Rajeshwar K, Tacconi N, Chenthamarakshan C (2001) Semiconductor-based composite materials: preparation, properties, and performance. Chem Mater 13:2765–2782
94. Cozzoli P, Manna L (2005) Tips on growing nanocrystals. Nature Mater 4:801–802
95. Yang J, Elim HI, Zhang Q, Lee JL, Ji W (2006) Rational synthesis, self-assembly, and optical properties of PbS-Au heterogeneous nanostructures via preferential deposition. J Am Chem Soc 128:11921
96. Dukovic G, Merkle MG, Nelson JH, Hughes SM, Alivisatos AP (2008) Photodeposition of Pt on colloidal CdS and CdSe/CdS semiconductor nanostructures. Adv Mater 20:4306–4311
97. Deka S, Falqui A, Bertoni G, Sangregorio C, Poneti G, Morello G, Giorgi M, Giannini C, Cingolani R, Manna L, Cozzoli PD (2009) Fluorescent asymmetrically cobalt-tipped CdSe@CdS Core@Shell nanorod heterostructures exhibiting room-temperature ferromagnetic behavior. J Am Chem Soc 131:12817–12828
98. Zanella M, Falqui A, Kudera S, Manna L, Casula MF, Parak WJ (2008) Growth of colloidal nanoparticles of group II–VI and IV–VI semiconductors on top of magnetic iron–platinum nanocrystals. J Mater Chem 18:4311–4317
99. Zhang JT, Tang Y, Lee K, Ouyang M (2010) Exciton-plasmon interactions in metal-semiconductor nanostructures. Science 327:1634–1638
100. Kim H, Achermann M, Balet LP, Hollingsworth JA, Klimov VI (2005) Synthesis and characterization of Co/CdSe core/shell nanocomposites: bifunctional magnetic-optical nanocrystals. J Am Chem Soc 127:544–546
101. Carbone L, Kudera S, Giannini C, Ciccarella G, Cingolani R, Cozzoli PD, Manna L (2006) Selective reactions on the tips of colloidal semiconductor nanorods. J Mater Chem 16:3952
102. Saunders AE, Popov I, Banin U (2006) Growth of colloidal nanoparticles of the group II-VI and IV-VI semiconductors on the top of magnetic ion-platinum nanocrystals. J Phys Chem B 110:25421
103. Menagen G, Mocatta D, Salant A, Popov I, Dorfs D, Banin U (2008) Selective gold growth on CdSe seeded CdS nanorods. Chem Mater 20:6900–6902

104. Carbone L, Jakab A, Khalavka Y, Sonnichsen C (2009) Light-controlled one-sided growth of large plasmonic gold domains on quantum rods observed on the single particle level. Nano Lett 9:3710–3714
105. Mokari T, Costi R, Sztrum CG, Rabani E, Banin U (2006) Formation of symmetric and asymmetric metal-semiconductor hybrid nanoparticles. Phys Stat Sol B 243:3952–3958
106. Khon E, Hewa-Kasakarage NN, Nemitz I, Acharya K, Zamkov M (2010) Tuning the morphology of Au/CdS nano-composites though temperature-controlled reduction of gold-oleate complexes. Chem Mater 22:5929
107. Costi R, Saunders AE, Banin U (2010) Colloidal hybrid nanostructures: a new type of functional materials. Angew Chem Int Ed 49:4878–4897
108. Zhang JT, Tang Y, Lee K, Ouyang M (2010) Tailoring light-matter-spin interactions in colloidal hetero-nanostructures. Nature 466:91–95
109. Lee J, Orazbayev A, Govorov AO, Kotov NA (2010) Solvent effect in dynamic superstructures from Au nanoparticles and CdTe nanowires: experimental observation and theoretical description. J Phys Chem C 114:1404–1410
110. Morfa AJ, Rowlen KL, Reilly TH, Romero MJ, Lagemaat VD (2008) Plasmon-enhanced solar energy conversion in organic bulk heterojunction photovoltaics. J Appl Phys Lett 92:013504
111. Oulton RF, Sorger VJ, Zentgraf T, Ma RM, Gladden C, Dai L, Bartal G, Zhang X (2009) Plasmon lasers at deep subwavelength scale. Nature 461:629–632
112. Jestl M, Maran I, Kock A, Beinstingl W, Gornik E (1989) Polarization-sensitive surface plasmon Schottky detectors. Opt Lett 14:719–721
113. Sheldon MT, Trudeau PE, Mokari T, Wang LW, Alivisatos AP (2009) Enhanced semiconductor nanocrystal conductance via solution grown contacts. Nano Lett 9:3676–3682
114. Maynadie J, Salant A, Falqui A, Respaud M, Shaviv E, Banin U, Soulantica K, Chaudret B (2009) Cobalt growth on the tips of CdSe nanorods. Angew Chem Int Ed 48:1814–1817
115. Drexhage KH, Wolf E (1974) Progress in optics. Amsterdam, The Netherlands, Vol. XII, p 163.
116. Achermann M (2010) Exciton-plasmon interactions in metal-semiconductor nanostructures. J Phys Chem Lett 1:2837–2843
117. Shimizu KT, Woo WK, Fisher BR, Eisler HJ, Bawendi MG (2002) Surface-enhanced emission from single semiconductor nanocrystals. Phys Rev Lett 89:117401
118. Farahani JN, Pohl DW, Eisler HJ, Hecht B (2005) Single quantum dot coupled to a scanning optical antenna: a tunable superemitter. Phys Rev Lett 95:17402
119. Bergman DJ, Stockman MI (2003) Phys Rev Lett 90:027402
120. Mertens H, Biteen JS, Atwater HA, Polman A (2006) Surface plasmon amplification by stimulated emission of radiation: quantum generation of coherent surface plasmons in nanosystems. Nano Lett 6:2622–2625
121. Okamoto K, Niki I, Shvartser A, Narukawa Y, Mukai T, Scherer A (2004) Surface plasmon enhanced light-emitters based on InGaN quantum wells. Nat Mater 3:601–605
122. Guo P-F, Wu S, Ren Q-J, Lu J, Chen Z, Xiao S-J, Zhu Y-YJ (2010) Phys Chem Lett 1:315–318
123. Gryczynski I, Malicka J, Jiang W, Fischer H, Chan WCW, Gryczynski Z, Grudzinski W, Lakowicz JR (2005) Surface-plasmon-coupled emission of quantum dots. J Phys ChemB 109:1088–1093
124. Pillai S, Catchpole KR, Trupke T, Zhang G, Zhao J, Green MA (2006) Surface plasmon enhanced silicon solar cells. Appl Phys Lett 88:161102
125. Muskens OL, Giannini V, Sanchez-Gil JA, Rivas JG (2007) Strong enhancement of the radiative decay rate of emitters by single plasmonic nanoantennas. Nano Lett 7:2871–2875
126. Wang Y, Yang T, Tuominen MT, Achermann M (2009) Radiative rate enhancements in hybrid metal-semiconductor nanostructures. Phys Rev Lett 102:163001
127. Noginov MA, Zhu G, Mayy M, Ritzo BA, Noginova N, Podolskiy VA (2008) Stimulated emission of surface plasmon polaritons. Phys Rev Lett 101:226806

128. Noginov MA, Zhu G, Belgrave AM, Bakker R, Shalaev VM, Narimanov EE, Stout S, Herz E, Suteewong T, Wiesner U (2009) Demonstration of a spaser-based nanolaser. Nature 460:1110–1112
129. Zheludev NI, Prosvirnin SL, Papasimakis N, Fedotov VA (2008) Lasing spaser. Nat Photonics 2:351–354
130. Englund D, Fattal D, Waks E, Solomon G, Zhang B, Nakaoka T, Arakawa Y, Yamamoto Y, Vuckovic J (2005) Efficient source of deterministically polarized single photons. Phys Rev Let 95:013904
131. Schaadt DM, Feng B, Yu ET (2005) Enhanced semiconductor optical absorption via surface plasmon excitation in metal nanoparticles. Appl Phys Lett 86:063106
132. Rand BP, Peumans P, Forrest SR (2004) Long-range absorption enhancement in organic tandem thin-film solar cells containing silver nanoclusters. J Appl Phys 96:7519–7526
133. Lee J, Hernandez P, Lee J, Govorov AO, Kotov NA (2007) Exciton-plasmon interactions in molecular spring assemblies of nanowires and wavelength-based protein detection. Nat Mater 6:291–295
134. Gupta JA, Knobel R, Samarth N, Awschalom DD (2001) Ultrafast manipulation of electron spin coherence. Science 292:2458–2461
135. Press D, Ladd TD, Zhang B, Yamamoto Y (2008) Complete quantum control of a single quantum dot spin using ultrafast optical pulses. Nature 456:218–221
136. Berezovsky J, Mikkelsen MH, Stoltz NG, Coldren LA, Awschalom DD (2008) Picosecond coherent optical manipulation of a single electron spin in a quantum dot. Science 320:349–352
137. Gómez DE, Vernon KC, Mulvaney P, Davis TJ (2010) Surface plasmon mediated strong exciton-photon coupling in semiconductor nanocrystals. Nano Lett 10:274–278
138. Khon E, Mereshchenko A, Tarnovsky AN, Acharya K, Klinkova A, Hewa-Kasakarage NN, Nemitz I, Zamkov M (2011) Suppression of the plasmon resonance in Au/CdS colloidal nanocomposites. Nano Lett 11:1792
139. Costi R, Saunders AE, Banin E, Angew U (2010) Colloidal hybrid nanostructures: a new type of functional materials. Chem Int Ed 49:4818–4897
140. Costi R, Saunders AE, Elmalem E, Salant A, Banin U (2008) Visible light-induced charge retention and photocatalysis and hybrid CdSe-Au nanodumbbells. Nano Lett 8:637–641
141. Zhao N, Liu K, Greener J, Nie Z, Kumacheva E (2009) Close-packed superlattices of side-by-side assembled Au-CdSe nanorods. Nano Lett 9:3077–3081
142. Scholes GD (2008) Insights into excitons confined to nanoscale systems: electron-hole interaction, binding energy and photodissociation. ACS Nano 2:523–537
143. Kelly KL, Coronado E, Zhao LL, Schatz GC (2003) The optical properties of metal nanoparticles: the influence of size, shape, and dielectric environment. J Phys Chem B 107:668–677
144. Link S, El-Sayed MA (1999) Size and temperature dependence of the plasmon absorption of colloidal gold nanoparticles. J Phys Chem 103:8410–8426
145. El-Sayed MA (2001) Some interesting properties of metals confined in time and nanometer space of different shapes. Acc Chem Res 34:257–264
146. Boernstein L (1998) Numerical data and functional relationships in science and technology. Group III, Condensed Matter, SubVolume C; Martienssen W (ed) Springer, Verlag
147. Dinger A, Petillon S, Grün M, Hetterich M, Klingshirn C (1999) Conduction band offset of the CdS/ZnSe heterostructure. Semi Sci Tech 14:595–598
148. Hewa-Kasakarage NN, El-Khoury PZ, Tarnovsky AN, Kirsanova M, Nemitz I, Nemchinov A, Zamkov M (2010) Ultrafast carrier dynamics in type II ZnSe.CdS.ZnSe nano- barbells. ACS Nano 4:1837–1844
149. Kreibig U, Vollmer M (1995) Optical properties of metal clusters. Springer, Berlin
150. Ahmadi TS, Logunov SL, El-Sayed MA (1996) Picosecond dynamics of colloidal gold nanoparticles. J Phys Chem 100:8053–8056

151. Logunov SL, Ahmadi TS, El-Sayed MAJ (1997) Electron dynamics of passivated gold nanocrystals probed by subpicosecond transient absorption spectroscopy. Phys Chem B 101:3713–3719
152. Yong KT, Sahoo Y, Choudhury KR, Swihart MT, Minter JR, Prasad PN (2006) Shape control on PbSe nanocrystals using noble metal seed particles. Nano Lett 6:709
153. Pacholski C, Kornowski A, Weller H (2004) Nanomaterials: site-specific photodeposition of silver on ZnO nanorods. Angew Chem Int Ed 43:4774
154. Mokari T, Aharoni A, Popov I, Banin U (2006) Diffusion of gold into in as nanocrystals. Angew Chem Int Ed 45:8001
155. Yong KT, Sahoo Y, Choudhury KR, Swihart MT, Minter JR, Prasad PN (2006) Control of the morphology and size of PbS nanowires using gold nanoparticles. Chem Mater 18:5965
156. Peng P, Milliron DJ, Hughes SM, Johnson JC, Alivisatos AP, Saykally RJ (2005) Femtosecond spectroscopy of carrier relaxation dynamics in a type II CdSe/CdTe tetrapod heteronanostructures. Nano Lett 5:1809–1813
157. Dooley CJ, Dimitrov SD, Fiebig T (2008) Ultrafast electron transfer dynamics in CdSe.CdTe donor-acceptor nanorods. J Phys Chem C 112:12074–12076
158. Lupo MG, Sala FD, Carbone L, Zavelani-Rossi M, Fiore A, Lüer L, Polli D, Cingolani R, Manna L, Lanzani G (2008) Ultrafast electron- hole dynamics in core/shell CdSe/CdS dot/rod nanocrystals. Nano Lett 8:4582–4587
159. Hewa-Kasakarage NN, Gurusinghe PG, Zamkov M (2009) Blue-shifted emission in CdTe/ZnSe heterostructured nanocrystals blue-shifted emission in CdTe/ZnSe heterostructured nanocrystals. J Phys Chem C 113:4362–4368